

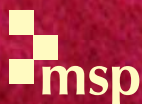
# Journal of Mechanics of Materials and Structures

**TUBULAR ALUMINUM CELLULAR STRUCTURES: FABRICATION AND  
MECHANICAL RESPONSE**

Ryan L. Holloman, Vikram Deshpande, Arve G. Hanssen, Katherine M. Fleming,  
John R. Scully and Haydn N. G. Wadley

**Volume 8, No. 1**

**January 2013**



## TUBULAR ALUMINUM CELLULAR STRUCTURES: FABRICATION AND MECHANICAL RESPONSE

RYAN L. HOLLOMAN, VIKRAM DESHPANDE, ARVE G. HANSEN,  
KATHERINE M. FLEMING, JOHN R. SCULLY AND HAYDN N. G. WADLEY

We explore a novel cellular topology structure based upon assemblies of square cross section tubes oriented in a cross-ply 2D and orthogonal 3D arrangements that can be tailored to support different combinations of through thickness and in-plane loads. A simple dip brazing approach is used to fabricate these structures from assemblies of extruded 6061-T6 aluminum alloy tubes and the through thickness compression of a variety of structures is investigated experimentally and with finite element modeling. We find that the 3D orthogonal structures have an approximately linear dependence of modulus upon relative density. However the strength has a power law dependence upon density with an exponent of approximately  $5/3$ . These cellular structures exhibit almost ideal plastic energy absorption at pressures that can be selected by adjustment of the vertical and in-plane tube wall thicknesses. A finite element model with a nonlinear hardening constitutive law is used to explore the buckling modes of the structure, and to investigate the relationship between cell topology, relative density, tube wall material properties and the cellular structures resistance to compression.

### 1. Introduction

Sandwich panel structures are widely used in stiffness dominated design where large bending stresses must be supported with minimum elastic deflection [Allen 1969]. In these scenarios, widely separated face sheets carry the primary loads and are constructed of light, stiff, strong materials such as light metals or fiber reinforced composites. When panel deflections are small, the mechanical performance is optimized by minimizing the core mass fraction [Zenkert 1995]. Since the flexural modulus of the sandwich panel increases with the square of the core thickness, the primary role of the core is to maintain separation of the faces and preserve the sandwich effect [Vinson 2001]. Cores for such applications can be made of low density materials such as Nomex with a hexagonal honeycomb cell topology [Bitzer 1997] or rigid polymer foams for less weight sensitive applications [Gibson and Ashby 1988; Mills 2007]. It is interesting to note that the development of these structures has been paced by advances in the adhesives used to strongly (and reliably) bond face sheets to the cores. More recently many other core options have emerged [Wadley 2006] including honeycombs with in-plane stretch resistant square [Wadley et al. 2007] or triangular [Wei et al. 2008] cell topologies, and flex honeycomb or lattice truss cores [Kooistra et al. 2008] for curved sandwich panels. Ways of making these cellular materials from engineering alloys such as high strength aluminum [Queheillalt et al. 2008; Kooistra et al. 2004] titanium [Queheillalt et al. 2000; Elzey and Wadley 2001; Moongkhamklang and Wadley 2010] and from composites have also been developed [Finnegan et al. 2007; Russell et al. 2008].

*Keywords:* cellular structures, 6061 aluminum, impact energy absorption.

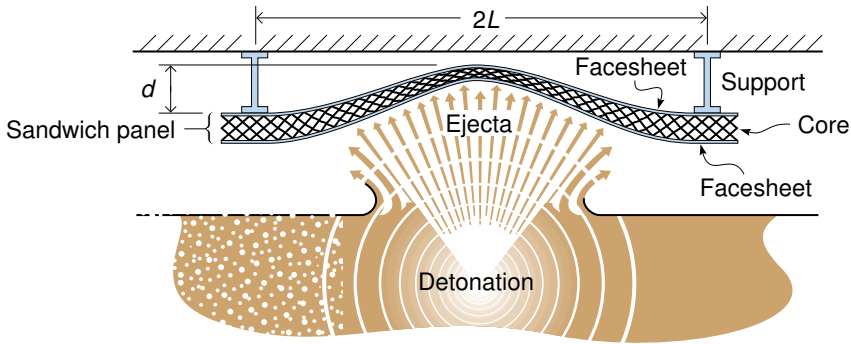


**Figure 1.** Example of a sandwich panel structure whose core undergoes localized compression, transverse shear, and membrane stretching during high intensity impulsive loading. The core in this example exhibits modest resistance to inplane stretching.

Sandwich panel structures have also attracted interest for impact energy absorption applications [Laurin and Vizzini 2005] and for reducing the dynamic deflections of structures that are subjected to high intensity dynamic loading [Vaziri et al. 2007]. Experimental studies have demonstrated significant reductions in panel deflections during shock loading under water [Wei et al. 2007], in air [Dharmasena et al. 2008] and when impacted by soil launched toward a panel by a buried explosion [Rimoli et al. 2011]. These studies reveal that the panel's out-of-plane deflection,  $d$ , scaled by the half span length,  $L$ , increases roughly linearly with the incident impulse  $I$  [Hutchinson and Xue 2005; Liang et al. 2007; McShane et al. 2007]. Under the most intense loadings, the deflections of edge clamped panels exceed the core thickness and the deformation of the panel changes to a combination of core crushing and in-plane stretching [Tilbrook et al. 2006]; see Figure 1. In this phase of the response, the resistance of the core to through thickness compression and in-plane stretching of the core and faces govern panel performance.

Sandwich structures intended for high intensity impulsive loading scenarios typically allocate about a third of the panels mass to the core to achieve the desired combination of core and face sheet responses [Wicks and Hutchinson 2001]. Foams [Reyes 2008], and tubes (both empty and foam filled) oriented axially to the crush direction [Hanssen et al. 2000a; Baumeister et al. 1997; Reid 1993] have been widely investigated for structural impact problems. These structures are highly compressible and can undergo compression at nearly constant stress to strains of 60% or more, making them efficient impact energy absorbers. However, they have little in-plane stretch or transverse shear resistance and are not optimally suited for the cores of edge supported sandwich panels subjected to high intensity loading. While honeycomb structures with square [Xue and Hutchinson 2006] or triangular [Gibson and Ashby 1997] cell topologies have shown promise for this application, (the webs resist compression and in the in-plane stretching), they are difficult to fabricate from the high performance alloys needed for many applications. Achieving the robust nodal connections between the core and face sheets is also problematic because of the small nodal contact area. It is difficult to independently vary, and thus tailor, the through-thickness and in-plane properties.

Here we investigate core topologies based upon 3D arrangements of square cross section, extruded tubes made from a heat treatable aluminum alloy. The tubes can be assembled in a 2D cross-ply, or 3D

orthogonal geometry. The in-plane tubes provide stretch resistance while the through thickness tubes resist compression. By using different wall thicknesses for the in-plane and through thickness tubes, it is possible to independently control the in-plane stretch resistance and the through thickness crush strength. The large nodal contact areas also improve load transfer within the core and between cores and face sheets. The topology affords multifunctionality [Evans et al. 2001] such as cross flow heat exchange via the open channels that extend within the structure [Tian et al. 2007]. We describe a simple method for the fabrication of tube core topology structures, and investigate their mechanical response under quasistatic compression loading. We find that a 3D orthogonal arrangement of tubes offers effective crushing resistance and appears well suited for impact energy absorbing applications.

## 2. Cell geometries and fabrication

To explore the design and fabrication of tube-bonded cellular structures we have investigated two rectangular cell topologies with and without tubes oriented in the loading direction and develop a method for their manufacture from extruded aluminum tubes.

**2.1. Cell geometry.** Rectilinear cellular tube structures can be assembled from square cross-section tubes to create the two topologies shown in Figure 2. The 2D structure in Figure 2(a) can be assembled by laying down a colinear layer of tubes each spaced a tube width apart. A second similarly spaced layer is then orthogonally placed on the first layer, and the assembly sequence repeated until a desired thickness is achieved. The 3D topology in Figure 2(c) can be assembled from the 2D structure by inserting additional

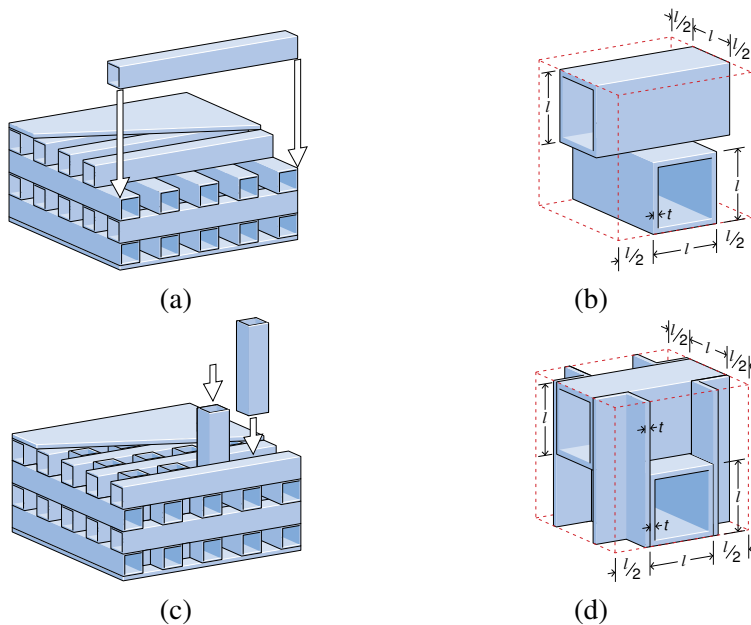


**Figure 2.** Examples of cellular structures fabricated from square extruded tubes. (a) 2D structure made by bonding 0/90 layers of colinear tubes. (b) The unit cell of the 2D structure. (c) A 3D tube structure where the through thickness gaps in the 0/90 assembly are filled with vertical tubes. (d) Unit cell of the 3D tube structure.

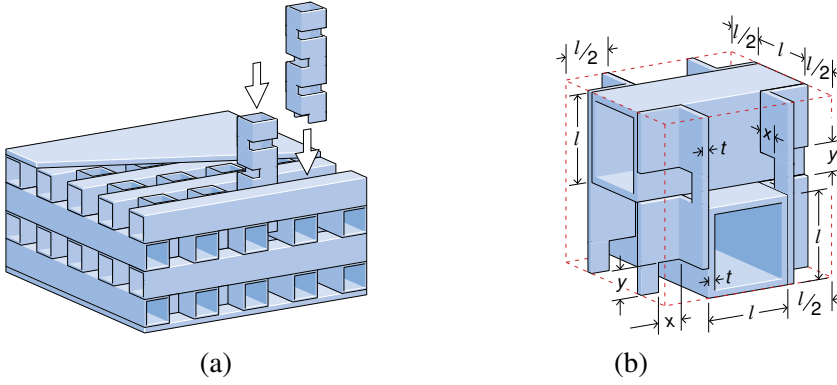


**Figure 3.** (a) A modified 3D structure in which the vertical tubes were notched to allow removal of salts used for dip braze bonding. (b) The unit cell of the modified 3D structure with the notch geometry incorporated. For all experiments reported here,  $x = y = 6.35$  mm.

tubes in the out of plane (vertical) void space between the cross-ply oriented tubes. The tubes can be bonded with polymeric adhesives or more robustly by dip or vacuum brazing. To facilitate complete fluid penetration during dip braze bonding of the structure to face sheets, the vertically inserted tubes can be notched as shown in Figure 3. In principle, the wall thicknesses of the tubes in each orthogonal direction can be different, enabling tuning of properties in the various directions.

The structures are periodic and their unit cells are shown in Figures 2(b), 2(d) and 3(b). The relative density,  $\bar{\rho}$ , of each topology is defined as the fraction of volume occupied by solid in each unit cell. The relationship between  $\bar{\rho}$ , the tube wall thickness ( $t$ ), and outer tube width ( $l$ ) for the 2D topology is given by

$$\bar{\rho} = \frac{2(l-t)t}{l^2}. \quad (1)$$

The 3D topology assembled from identical tubes in all three directions has a relative density

$$\bar{\rho} = \frac{3(l-t)t}{l^2}. \quad (2)$$

However, use of notched vertical tubes, with rectangular notches of length  $x$  and height  $y$ , results in a reduced relative density for the 3D assemblies

$$\bar{\rho} = \frac{2 * t_v^2 (y - 2l) - t_v (2xy + l(y - 4l)) - 8t_h (t_h - l)l}{4l^3} \quad (3)$$

where the in-plane and through thickness oriented tubes can have different wall thicknesses of  $t_h$  and  $t_v$ , respectively. Figure 2 shows that when the cellular tube structures are bonded to face sheets to create sandwich panels, they have a large core to face sheet interfacial area with potentially beneficial consequences for the robustness of intensely loaded panels.

**2.2. Cellular tube structure fabrication.** Initial investigations of the mechanical response of a 2D core (described in Section 4) revealed unstable collapse and poor energy absorption characteristics during compressive loading. Only the 3D geometry is therefore examined in detail. The 3D orthogonal geometry

Topology	Average in-plane tube wall thickness (mm)	Average in-plane tube width (mm)	Average out of plane tube wall thickness (mm)	Average out of plane tube width (mm)	Relative density, $\bar{\rho}$
3D	3.47	19.05	3.47	19.05	42.7
3D	3.27	19.05	1.52	19.05	35.1
3D	1.53	19.05	3.30	19.05	28.6
3D	1.45	19.05	1.45	19.05	20.1
3D	0.74	11.48	0.74	11.48	11.6
3D, not notched	1.44	19.05	1.44	19.05	21.0
2D	1.70	19.05	-	-	16.3
1D array	-	-	1.52	19.05	6.7

**Table 1.** Tube geometries and predicted relative densities for tube-based cellular structures.

assembled from tubes of the same size, behaved well under compressive loading, and so samples were also assembled from tubes of various wall thickness and outer tube widths to investigate the effect of these geometric parameters upon energy absorption and collapse mechanisms. The geometries of all the structures investigated are summarized in [Table 1](#). Since there was variability in the wall thickness, the wall thickness of fifty tubes was measured and the mean thickness was calculated and reported in the table. The standard deviation in tube wall thickness was  $\pm 0.14$  mm. These wall thickness variations were accounted for by the introduction of imperfections in the FE models described later ([Section 5](#)).

Samples of each cell topology were fabricated from square cross-section, 6061-T6 aluminum alloy extrusions using a simple dip brazing process followed by an aging heat treatment. Square cross-sectional extruded 6061-T6 aluminum alloy tubes were obtained from Argyle Industries Inc. (Branchburg, NJ, USA). To facilitate compression testing, a face sheet was attached to opposing sides of the samples to create sandwich panels. The 4.76 mm thick 6061-T6 aluminum alloy face sheet material was supplied by BMG Metals (Richmond, VA, USA).

A schematic illustration of the fabrication process for making the 3D orthogonal topology structure is shown in [Figure 4](#). An analogous sequence was used for the 2D topology. All the test structures were dip brazed using a facility and process developed at Coleman Microwave Co. (Edinburg, VA, USA). This process involves a prebrazing cleaning, dip brazing, and a postbrazing heat treatment [[ASM 2003](#)]. The AA 6061-T6 parts were first subjected to a degreasing/chemical deoxidation process to remove the thick oxide films that form during extrusion processing and subsequent heat treatments. This involved soaking the tubes in a degreasing solution (Hurrifsafe 950 supplied by PCI of America of Rockville, Md, USA) at 65° to 82°C to remove hydrocarbon residues. After rinsing in warm water, the parts were dipped in a caustic bath (Isoprep 35 supplied by MacDermid of Denver, CO) for 30 seconds to lightly etch the surface. After a second warm water rinse, the parts were dipped for 30 seconds in a neutralizing acid bath (Gil-Sparkle C solution diluted 50% with de-ionizing water). The parts were again rinsed in a warm water bath before dipping for 45 seconds in a deoxidizing solution containing ferric sulfate, sulfuric acid, and nitric acids followed by rinsing in warm water and air drying. Once cleaned, the extrusions were assembled into the appropriate sandwich geometry. During assembly, Lynch Metal (Union, NJ) grade 4047 Al-Si filler foil was applied to the surfaces of the cellular structure as shown in [Figure 4](#).

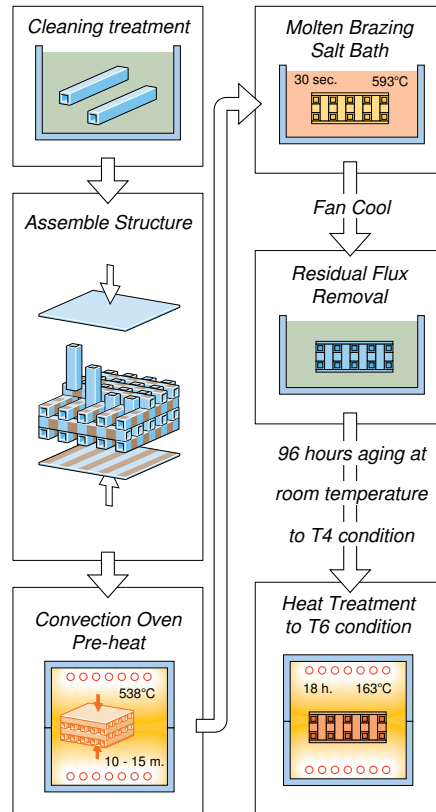


**Figure 4.** A process flow chart for the manufacturing sequence used to fabricate the cellular tube structures.

Filler alloy 4047 was used due to its improved fluidity (wetting action) and for minimizing solidification cracking. A bead of AA 4145 filler paste (Omni/Lucas Milhaupt grade LTB 37-SSK) was also applied to any small gaps within the assembly. In the case of the 3D structures, it is assumed that AA 4145 was used in very limited quantities and only along small joints at the edge of the 3D structure. [Table 2](#) summarizes the compositions of the AA 6061, AA 4047, and AA 4145 alloys, whose compositions and braze process conditions governed the microstructure [[Fleming et al. 2012](#)]. It should be noted that perfect tube alignment for all tested structures was difficult to maintain with the fabrication method used here. The tubes slid and it was difficult to attain perfect alignment even with clamping the face sheets. Both tube wall thickness variability and misalignment are imperfections that trip tube buckling modes during subsequent compression testing.

After assembly, the cellular structure was clamped to the top and bottom face sheets and the entire assembly mounted on a rack for dip brazing. The assembly was preheated for 10–15 minutes at 538°C (just slightly below the brazing temperature) in a hot air convection oven to remove moisture [[ASM 2003](#)]. The structures were then quickly transferred to a 593°C bath of molten brazing flux (Alu-braze 960, Park Metallurgical, Detroit, MI) for approximately 30 seconds, this acted as both a heating medium and deoxidizer. During this emersion, the molten braze alloy flowed (by capillary action) to fill the joints. After removal

Material	Composition (wt%)							
	Si	Cu	Mg	Mn	Fe	Cr	Zn	Mg/Si
AA 6061	0.4–0.8	0.15–0.4	0.8–1.2	0–0.15	0–0.7	0.04–0.35	0–0.25	0.5–1.5
AA 4047	11.0–13.0	0.3	0.1	0.15	0–0.8	0	0–0.2	0.009max
AA 4145	9.3–10.7	3.3–4.7	0.15	0–0.15	0–0.8	0	0–0.2	0.016max

**Table 2.** Composition of extruded material (AA 6061) and filler materials used to braze the tube profiles [Hatch 1984; Braithwaite 2008].

from the molten flux bath, molten salt was drained from the structure, and it was fan cooled to room temperature at rates ranging from 0.08 to 0.32 K/s, depending on the size of the structure. The structure was then soaked in hot-agitated water and Gil-Sparkle C solution with a 50% de-ionized water. After these fabrication steps, the structure was slow-aged at room temperature for 96 hours to the T4 condition and then peak hardened (to the T6 condition) by ageing at 163°C for 18 hours followed by water quenching.

### 3. Materials characterization

**3.1. Microstructure characterization.** Micrographs of the parent alloy and brazed regions of one of the structures studied here are shown in Figure 5, all samples were electropolished [Fleming et al. 2012] prior to imaging. Figure 5(a) shows a backscattered SEM micrograph of the tube wall material for a region more than 125  $\mu\text{m}$  from a brazed joint. In the post brazed and heat treated condition, the tube wall

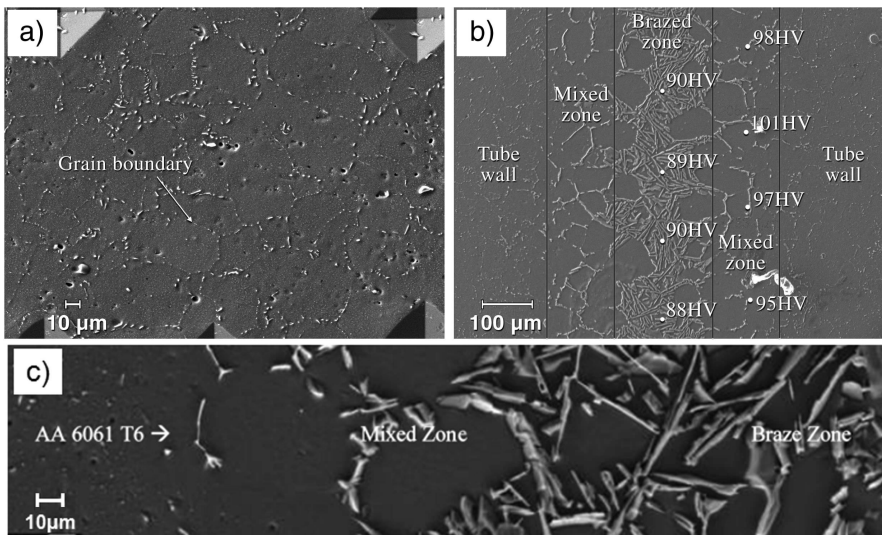


**Figure 5.** SEM images of the post-brazed and heat treated AA 6061-T6 material. (a) Backscatter electron image of the extruded tube wall showing precipitate phases decorating the grain boundaries. (b) The brazed region between two tubes showing silicon rich phases. Microhardness values are shown within the brazed and mixed zones. (c) A higher magnification view of the brazed and mixed zone regions.

material has an average grain size of  $20\ \mu\text{m}$ . The grain boundaries were decorated by large  $\beta\text{-Mg}_2\text{Si}$  and  $\text{Q-Al}_4\text{Cu}_2\text{Mg}_8\text{Si}_7$  phase precipitates, as predicted in [Chakrabarti and Laughlin 2004]. Fleming et al. [2012] has conducted a detailed examination of the microstructure evolutions accompanying the dip braze bonding process used here. The large  $\beta$ -phase grain boundary particles are consistent with the time-temperature transformation curves calculated by Fleming and the slower than normal rate of cooling after brazing. The brazed regions between the tubes, Figure 5(b) consisted of a eutectic structured region and a transition zone to the parent alloy microstructure. Within the brazed joint, the AA 4047 braze foil had fully melted and an fcc aluminum solid solution and diamond cubic silicon eutectic microstructure had formed upon cooling. Both  $\beta$  and  $\text{Q-Al}_4\text{Cu}_2\text{Mg}_8\text{Si}_7$  phases were predicted [Fleming et al. 2012] to be responsible for the strengthening in this region. The Vickers microhardness in the brazed and mixed regions was measured to be approximately 90 HV30 and 98 HV30, respectively; equivalent to tensile strengths of 285 and 300 MPa. In the mixed zone on either side of the original braze foil location, Figure 5(c), resolidified AA 6061 formed coarse grains with Al-Si eutectic at solidification boundaries. Kinetic models and composition profiles [ibid.] have shown that significant outward diffusion of silicon and inward diffusion of magnesium had occurred in a zone that extended  $125\ \mu\text{m}$  from the edge of the brazed zone. Strengthening in this region resulted from precipitated Si, as well as  $\beta$ , and Q phase precipitation in Al-rich phase [ibid.]

**3.2. Alloy mechanical properties.** An optical image of a polished cross section cut from a 3D structure is shown in Figure 6. Microhardness measurements were made at various locations (all further than  $125\ \mu\text{m}$  from any brazed region) to investigate the local strength of the post brazed/artificially age hardened

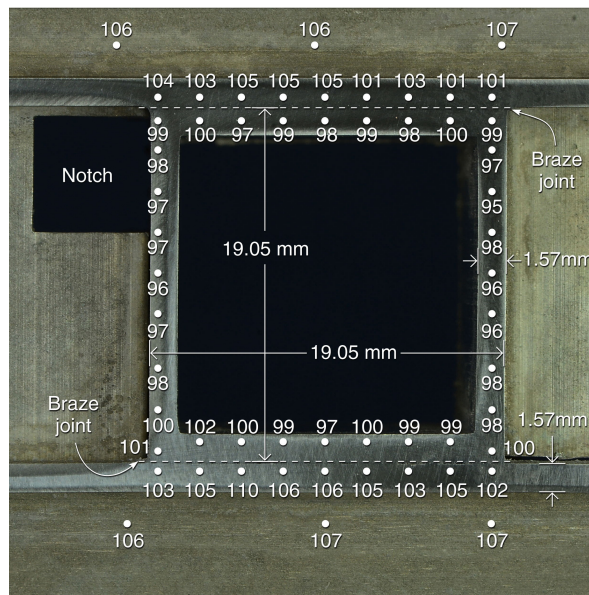


**Figure 6.** A photograph of a polished cross sectional slice through the 3D tube structure with measured Vickers microhardness values superimposed. A notch in one of the vertically oriented tubes can be seen in the upper left. All microhardness measurements are located in the AA 6061-T6 extrusion region.

extrusion region of the structure. These hardness values and approximate location of the measurement are shown in [Figure 6](#). The measured Vickers microhardness lay in the range of  $102 \pm 7.5$  HV30; equivalent to an alloy tensile strength of approximately 330 MPa, which is consistent with the T6 condition of the 6061 alloy. Indents made in the outer surface of the tube wall, indicated a hardness that deviated very little from 107 HV. However, when measured on a plane transverse to the extruded direction, the microhardness was roughly 10 HV smaller, and fluctuated between 95 HV and 102 HV. The microhardness indentation diameter was about 0.1 mm, while half the tube wall thickness was 0.8 mm. As a result the distance to the free surface from the middle of the tube wall was about eight times the indent diameter, and proximity to the free surface may have reduced lateral constraint during indentation. Hardness measured in the same orientation near the two (horizontal) brazed joints, indicated a hardness that varied between 101 and 110 HV consistent with better lateral constraint. We conclude that the strength of the tube wall alloy after brazing was approximately isotropic and independent of orientation.

Quasistatic tensile tests were used to determine the stress-strain response of the post-brazed and T6 aged 6061 tube wall alloy. The tensile test specimens were cut so that the loading direction was in the axial (extrusion) direction of the orthotropic tube material. The test coupons were prepared according to ASTM standard B557-06 and tested on a 50 kN screw driven universal testing machine (Instron Model 4208, Instron Corp, Canton, MA, USA) at 25°C at a strain rate  $\dot{\epsilon}$  of  $10^{-4} \text{ s}^{-1}$ . The specimen's axial displacement was determined with a laser extensometer (Electronic Instrument Research, Model LE-01, Irwin, PA, USA). The specimens were tested to failure and the Cauchy stress,  $\sigma_c$  and the logarithmic strain  $\epsilon_L$ , up to diffuse necking were calculated from

$$\sigma_c = \frac{F}{A_0(1 + \epsilon)}, \quad \epsilon_L = \ln \frac{L_2}{L_1} \quad (4)$$

where  $F$  is the force,  $A_0$  is the initial cross section of the tensile coupon,  $\epsilon$  is the engineering strain,  $L_1$  the initial gauge length and  $L_2$  the extended length.

To verify that material in the post brazed 3D orthogonal assembly had the same mechanical properties throughout its interior, tests were performed on material extracted from the walls of tubes located at the surface and the interior of the sample. Two samples from each location within a 3D cellular structure were obtained and tested. In addition, the AA 6061-T6 face sheet material was also tested in the rolling and transverse directions. [Figure 7](#) shows the cauchy stress-logarithmic strain curve for one of the tube wall material samples. This curve was subsequently used to deduce the material properties for the numerical simulations of the 3D orthogonal assembly. A summary of the mechanical test results for all the samples is shown in [Table 3](#). It is evident that there is little variation in the mechanical properties within the tube structure, and the ultimate strengths are consistent with the microhardness measurements.

The mechanical response of the brazed joint was also investigated using a lap shear test in accordance with test standards specified by ASTM D1002-05. The test specimens were cut in the length direction of the extruded tube and underwent the same brazing and age-hardening process described in [Section 2.2](#). Tests were conducted at a strain rate of  $10^{-5} \text{ s}^{-1}$  in the specimens gauge area. In three tests, the AA 6061-T6 material failed prior to the braze joint near the grips at a tensile stress of 247 MPa. The corresponding shear stress within the joint at the point of material failure was measure to be 165 MPa. Since no nodal fracture was observed at the brazed lap joint during these tests, the nodes of the adjacent tubes in the FE models ([Section 5](#)) were merged prior to simulations.

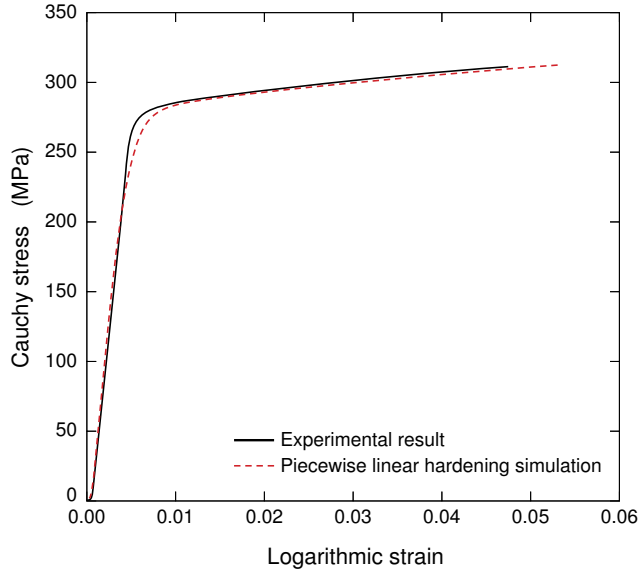


**Figure 7.** Measured true stress-logarithmic strain curve for post-brazed and fully age hardened AA 6061-T6 tube wall material tested in uniaxial tension to fracture at room temperature. The stress-strain curve predicted by a piecewise linear hardening constitutive model used in subsequent simulations is also included.

Direction	Modulus, $E_s$ (GPa)	Yield strength, $\sigma_{02}$ (MPa)	Ultimate strength, $\sigma_u$ (MPa)	Total strain to failure $\epsilon_f$ (%)
Exterior region of 3D structure				
Axial	70.5	278.2	310.5	5.3
Axial	69.9	280.9	311.5	5.1
Interior region of 3D structure				
Axial	68.5	284.5	313.6	4.9
Axial	68.3	283.2	312.8	4.9
Face sheet material				
Transverse	69.4	265.9	346.8	12.5
Rolling	71.4	281.4	344.3	12.7

**Table 3.** Mechanical properties of 3D orthogonal structure and face sheet.

#### 4. Compressive response of cellular structures

The compressive stress strain response of the cellular structures were measured following the guidelines of ASTM C 365/C for sandwich panel testing at an applied engineering strain rate of  $10^{-4} \text{ s}^{-1}$ . A laser extensometer was used to measure the compressive displacement and thus nominal strain.

**4.1. The 2D cellular structure.** The out of plane compressive response of the 2D structure with  $\bar{\rho} = 16.3\%$  is shown in Figure 8. The stress linearly increased with an elastic modulus (measured during

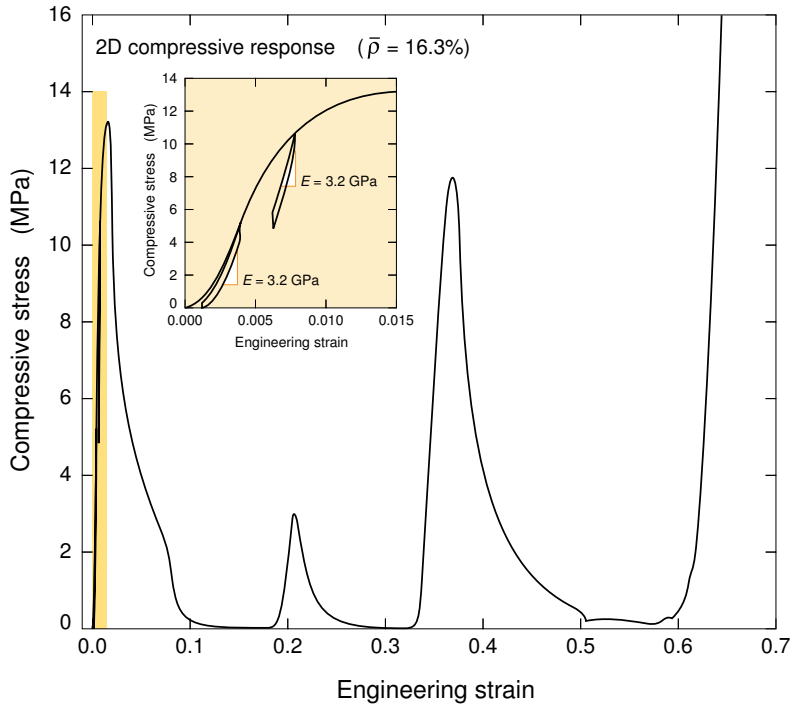


**Figure 8.** The compressive stress-strain response of a 2D cellular structure with a relative density of 16.3%. The inset shows an expanded view of the nominally elastic loading region of the test where the unloading modulus was measured.

unloading) of 3.2 GPa until reaching an initial peak of 13.2 MPa. Continued loading resulted in rapid softening and a significant period of compression at almost no stress. This was then followed by a second

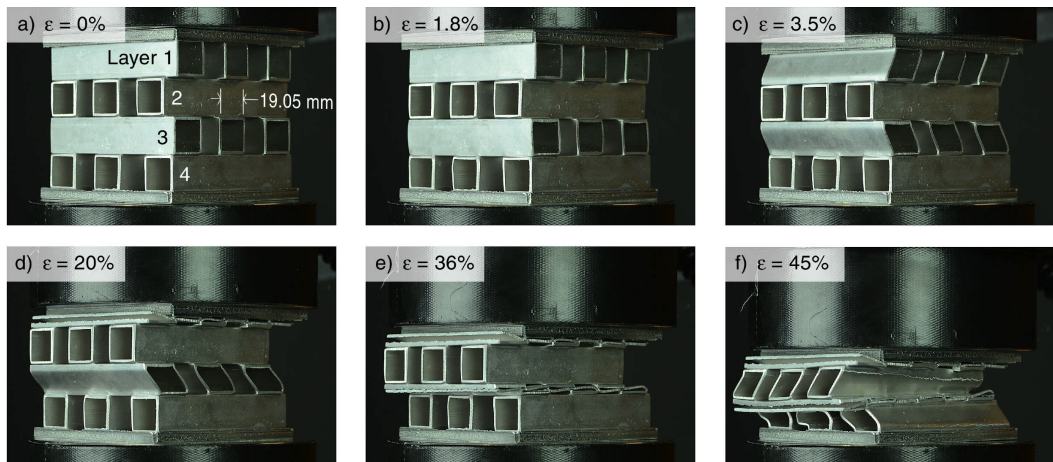


**Figure 9.** A photographic sequence showing the unstable collapse modes of a 2D cellular structure with a relative density of 16.3%.

rise in stress to a peak value of 3.1 MPa at a strain of 0.19 followed again by rapid softening. A third stress peak was observed with a maximum stress of 11.8 MPa at a strain of 0.35. Further loading again resulted in rapid softening until densification set in at a strain of 0.64.

Figure 9 shows a series of photographs of the 2D structure at various stages of the test. A comparison of parts (a) and (b) shows that the initial peak in strength was controlled by concertina buckling of layers 1 and 3 in which the tubes on either side of a horizontal plane rotate in opposite directions forming a chevron pattern; see Figure 9(c). Part (d) indicates that the second stress peak results from the complete collapse of layer 1. Examination of parts 9(e) and 9(f) show that the third stress peak resulted from collapse of layers 2 and 4 by the concertina buckling mode. Some variability of response was also observed. In some tests, the stress-strain response exhibited only two peaks that resulted from simultaneous collapse of layers 1 and 3, and then layers 2 and 4. Apparently small imperfections in the structure influenced the details of the buckling sequence, but not the generally unstable response of this structure.

The total absorbed (plastically stored) energy per unit volume,  $E_v$ , is obtained from the area under the stress-strain curve shown in Figure 8. The integration is usually terminated at the densification strain,  $\epsilon_D$  defined here as the strain where the flow stress reaches the initial yield stress ( $\epsilon_D = 0.64$  for this sample). This gave an energy absorbed per volume,  $E_v = 1.2 \times 10^6 \text{ J/m}^3$ . Dividing this by the core density  $\bar{\rho}\rho_s = 0.163 \cdot 2.7 \times 10^3 \text{ kg}\cdot\text{m}^{-3} = 440.1 \text{ kg}\cdot\text{m}^{-3}$  (where  $\rho_s$  is the density of the solid) gave an energy absorbed per unit mass,  $E_m = 2.72 \text{ J/g}$ . If the stress achieved at the first peak had remained constant until densification, the energy absorbed per unit mass in the 2D structure would have been the theoretical limit,  $E_m = 19.1 \text{ J/g}$ . Defining the energy absorbing efficiency as the ratio of measured energy absorption,  $E_m$ , versus the theoretical estimate for  $E_m$ , the 2D structure has an energy absorption efficiency of 14.2%. The low efficiency is a result of the unstable buckling response of the structure and makes the 2D core poorly suited for impact energy absorption applications. It was therefore investigated no further.

**4.2. The 3D structure.** The 3D cellular structures defined in Table 1 had relative densities of 42.7, 20.1, and 11.6% and were made of tubes of identical wall thickness in each orthogonal direction. The 20.1%

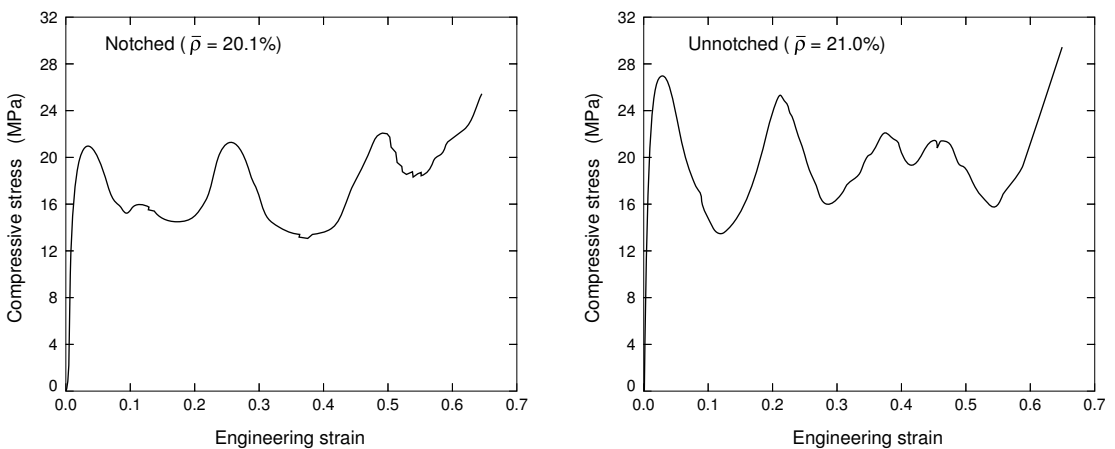


**Figure 10.** A comparison of the compressive stress-strain responses for 3D cellular structures assembled using notched (left) and unnotched (right) vertical tubes. The small difference in relative density results from removal of the notch material.

relative density structure represents the 2D structure in [Section 4.1](#), but with a notched tube inserted into the void of the colinearly aligned tubes, [Figure 3\(a\)](#). Its out of plane compressive response is shown in [Figure 10](#), left. The structures unload modulus during initial loading was 3.1 MPa. It reached an initial peak in strength of 20.9 MPa and then underwent moderate softening before hardening twice more to reach a strength about equal to that of the first peak. The sample then began to densify at a strain  $\epsilon_D = 0.61$ . The notched structure had an absorbed energy per unit volume,  $E_v = 10 \times 10^6 \text{ J/m}^3$  and an energy absorbed per unit mass of  $E_m = 19.2 \text{ J/g}$ . Its energy absorption efficiency was 81.0%.

To ascertain the effect of the notching, an otherwise identical cellular structure to that with a relative density of 20.1% was fabricated without notches in the through thickness tubes, and its compressive stress-strain response is shown in [Figure 10\(b\)](#). The slightly higher relative density of the unnotched structure (21.0%) was due to additional mass of the unnotched vertical tubes. It can be seen that notching

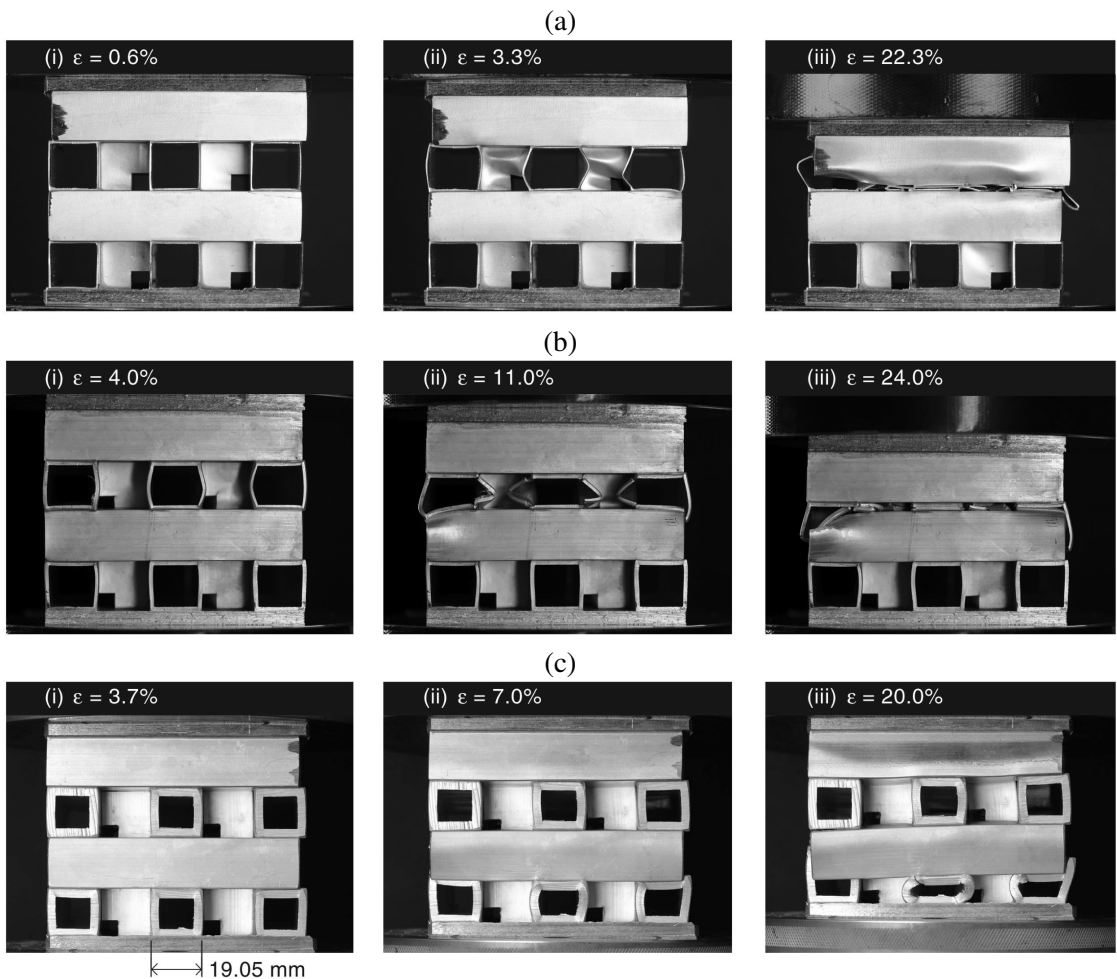


**Figure 11.** Photograph sequence of the collapse modes for 3D structures with relative densities of (a) 11.6, (b) 20.1, and (c) 42.7%. The strains at which each photograph was taken are indicated on [Figure 12](#).

reduced the initial peak strength of the 3D structure from 27.1 MPa to 20.9 MPa but also reduced the amplitude of the stress fluctuations. The energy absorbed per unit volume for the unnotched sample  $E_v = 12.45 \times 10^6 \text{ J/m}^3$  while  $E_m = 21.94 \text{ J/g}$ , which were both higher than those of the notched structure. However, the large stress drops observed in the sample with no axial tube notches reduced its energy absorption efficiency from 81.0 to 72.3%.

A photograph of the notched 3D structure with a relative density of 20.1% taken at the first peak in stress (at a strain of 0.04) is shown in Figure 11(b)(i). The drop in strength at the first peak resulted from the onset of buckling of the set of tubes oriented in the through thickness direction. This was nucleated at the notches in the tubes shown in the photographs of Figure 11(b). Continued loading resulted in softening to a relatively constant stress of approximately 15 MPa, Figure 12. At this stage, the buckles were fully formed in the through thickness tubes, and the side walls of the cross-ply tubes then began to buckle, Figure 11(b)(ii). This was accompanied by a second rise in stress at a strain of 0.21 that reached a peak value of 21.8 MPa as densification of layer 2 occurred, Figure 11(b)(iii). This process was repeated until each of the four cross-ply tube layers had densified at a strain  $\epsilon_D = 0.61$ .

The out of plane compressive response for cores with three different relative densities is compared in Figure 12. The ultimate peak strength of the 42.7, 20.1, and 11.6% relative density structures were

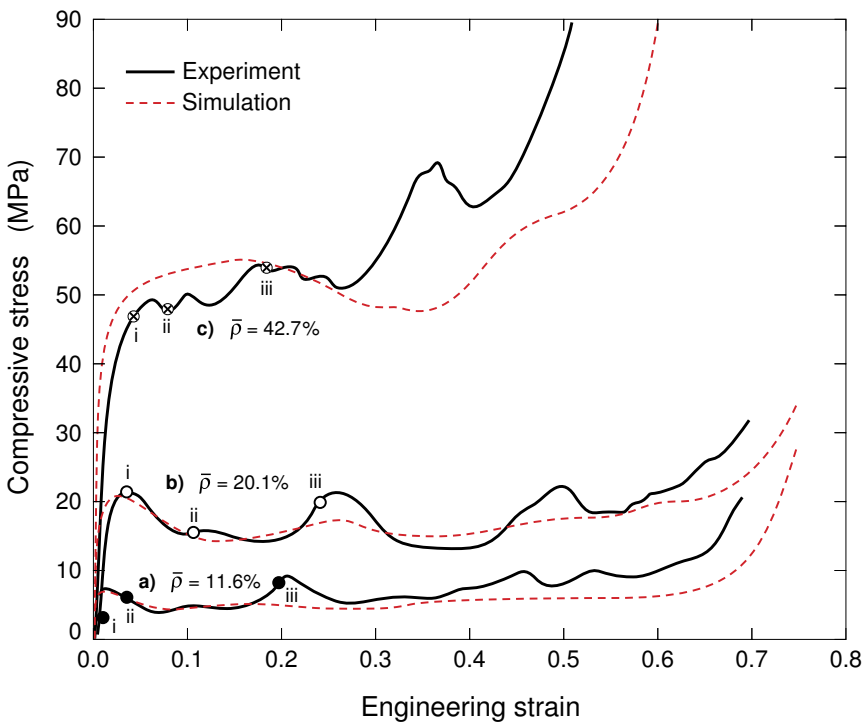


**Figure 12.** The compressive stress-strain responses of notched 3D cellular structures made from uniform wall thickness tubes with relative densities of 11.6, 20.1 and 42.7%. The structures exhibit a relatively flat stress-strain response after initial yield until attainment of a density dependent “densification strain” whereupon the stress rises sharply. The dashed curves correspond to FEA simulations discussed later.

Topology	Relative Density, $\bar{\rho}$	Peak stress, $\sigma_p$ (MPa)	$\epsilon_D$	$E_v$ (MJ/m <sup>3</sup> )	$E_m$ (J/g)	Theoretical $E_m$ (J/g)	Energy absorbing efficiency
3D	42.7	69.1	0.45	24.4	21.2	29.4	0.73
3D	35.1	53.3	0.51	23.8	25.1	27.5	0.91
3D	28.6	36.8	0.50	14.7	19.0	23.1	0.82
3D	20.1	21.8	0.61	10.4	19.2	23.7	0.81
3D	11.6	9.7	0.59	3.9	12.7	13.7	0.92
3D, no notch	21.0	27.1	0.63	12.5	21.9	30.1	0.72
2D	16.3	13.2	0.64	1.2	2.7	19.1	0.14
1D array	6.7	4.7	0.72	1.7	18.0	35.2	0.51

**Table 4.** Energy absorption values for tested tubular cellular structures.

69.1, 21.8, and 9.7 MPa respectively, and was controlled by buckling of the through thickness tubes, [Figure 11\(a\)–\(c\)](#). This buckling is clearly seen in [Figure 11\(a\)\(ii\)](#). Further collapse results from the folds in the vertical tube walls buckling into the cross-ply oriented tubes. The stress-strain curves of all three structures exhibit relatively constant stress until their (density dependent) densification strain was reached. [Table 4](#) summarizes the measured mechanical properties for all the samples.

**4.3. Effect of tube wall thickness.** [Figure 13\(a\)](#) shows the stress-strain responses of 3D structures in which the wall thicknesses of the in- and out-of-plane tubes were different. Recall that the 3D structure with equal tube thickness in all directions had a relative density of 42.7%. Its stress-strain response was shown in [Figure 11\(c\)](#). The wall thickness of just the out-of-plane tubes was reduced by a half, and the relative density decreased to 35.1% (82% of the isotropic structure), but the strength dropped by only 5%, [Figure 13\(a\)](#). A larger decrease in strength occurred when only the in-plane tube wall thicknesses were reduced by one half (while keeping the out-of-plane tubes at the original wall thickness). In this case, the relative density decreased to 28.6% (66% of the isotropic structure) and the peak strength was reduced by approximately 54%. From the images in [Figure 13\(b\)](#) and (c), the initial peak strength is seen to be controlled by a similar mechanism to that observed in isotropic samples with identical tube wall thicknesses. We also note that the structures with relative densities of 35.1% and 28.6% had excellent energy absorbing characteristics, with efficiencies of 91% and 82%, respectively; see [Table 4](#).

**4.4. Tube interactions.** To experimentally investigate possible interactions between tubes in the in- and out-of-plane directions, only the colinearly aligned (in-plane) tubes from the 3D structure with a relative density of 16.3% were tested in out-of-plane compression, [Figure 14\(a\)](#). The vertical notched tubes in this colinear tube structure were then also tested in (axial) compression. The response of this 1D array structure is shown in [Figure 14\(b\)](#). The stress-strain response for a 3D structure made by combining both sets of tubes is shown in [Figure 14\(c\)](#). The in-plane and out-of-plane tube cells have initial peak strengths of 13.2 and 4.7 MPa, respectively. The addition of these strengths (17.9 MPa) is seen to be less than that of the fully assembled 3D structures first peak (20.8 MPa). The experiment indicates the existence of a synergistic interaction between the colinear aligned and vertical tubes. In the same way that the peak strength of the 3D assembly cannot be reproduced by summation of the colinear and vertical

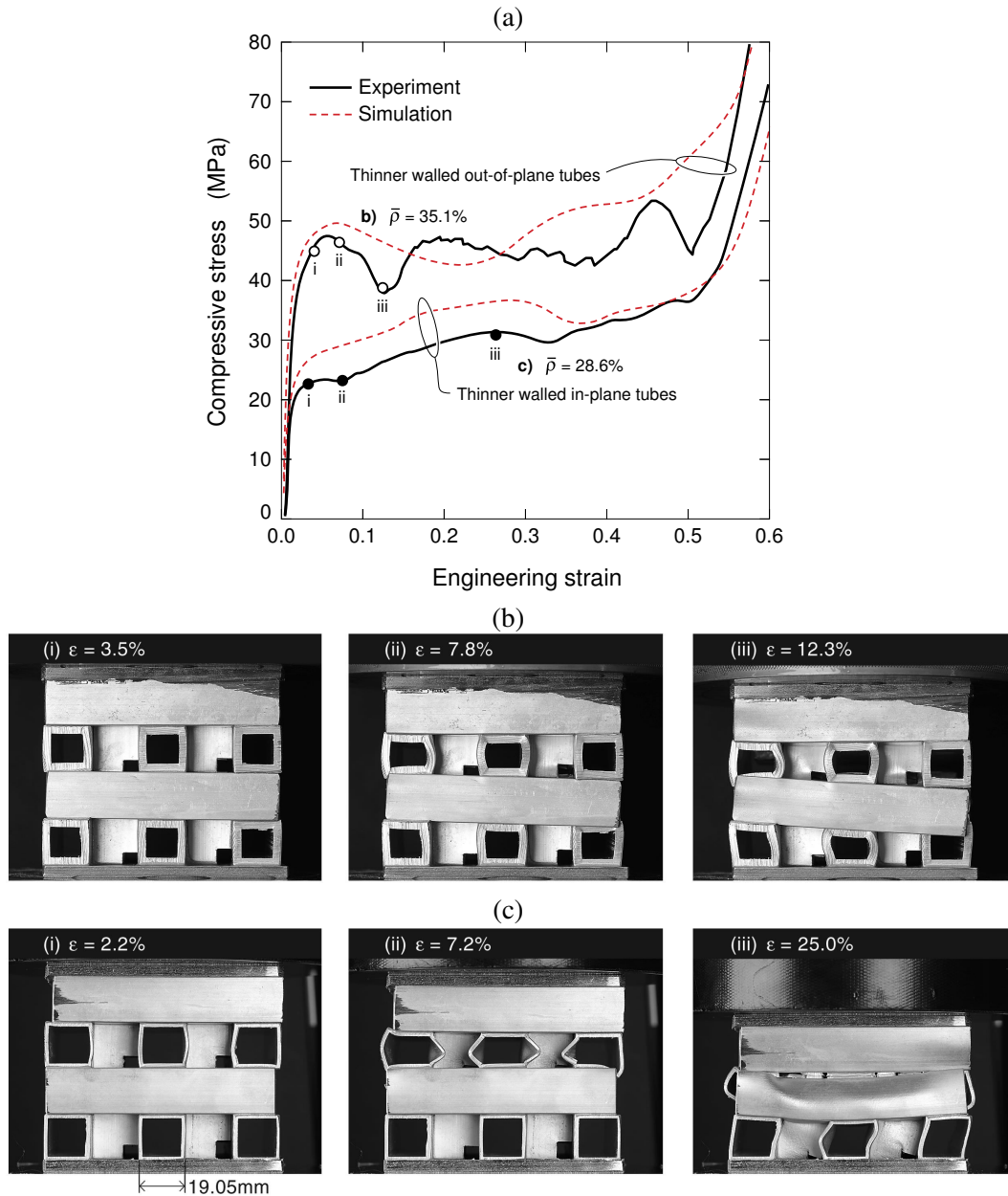


**Figure 13.** (a) The compressive stress-strain responses for notched 3D cellular structures in which the tube wall thicknesses in the vertical and horizontal directions were different. (c) The sample with a relative density of 28.6% density used in-plane tubes with a reduced wall thickness (of 1.57 mm). (b) The sample with a relative density of 35.1% was constructed using vertical tubes with a reduced thickness of 1.57 mm. The dashed curves correspond to FEA simulations discussed later. (b) and (c) show the collapse modes of the two structures. The in-plane tubes buckle first in (c) while the vertical tubes initiate failure in (b).

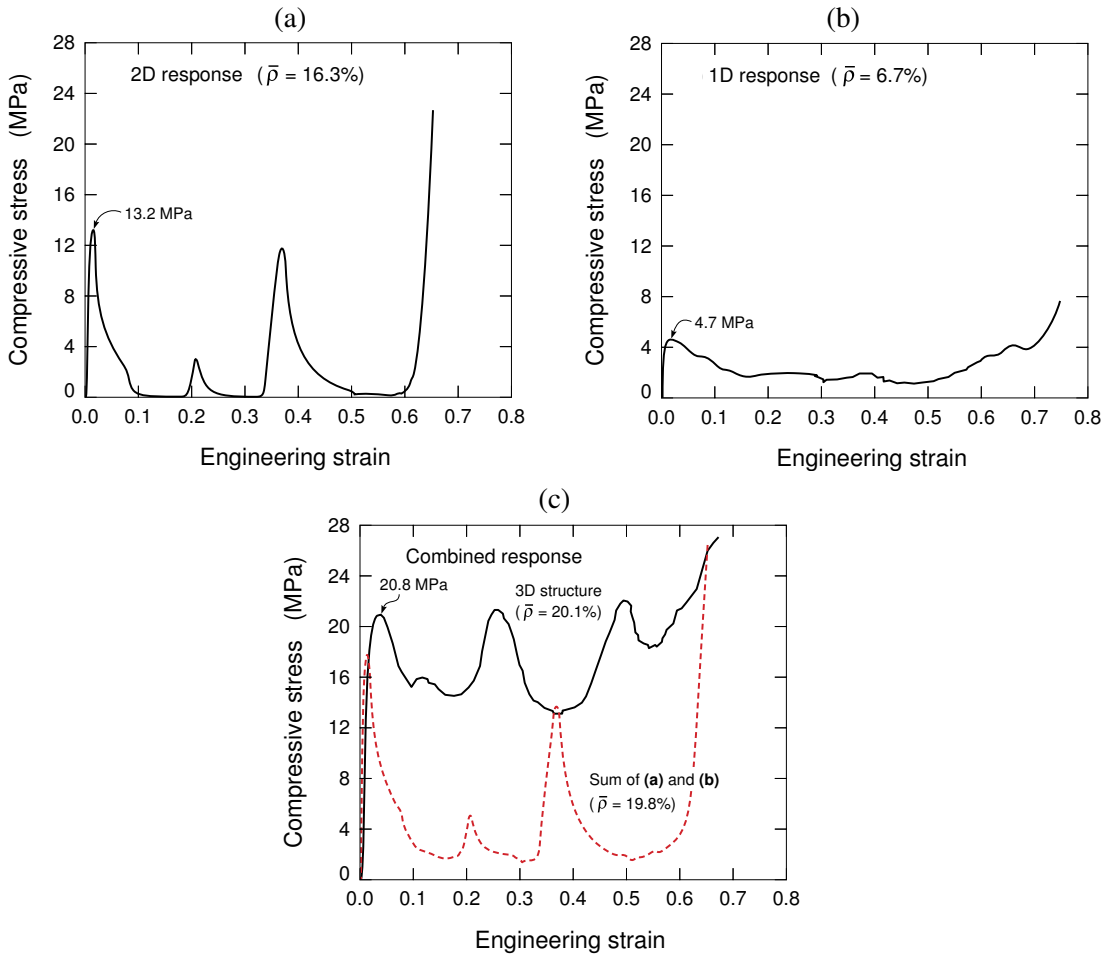


**Figure 14.** Measured stress-strain curves for a structure composed of (a) colinear aligned (0/90) tubes and (b) only the vertical tubes used in the 3D assembly. (c) Compares the summed response of (a) and (b) with that measured for the 3D structure. Note the considerable increase in energy storage of the 3D structure.

tubes acting separately, the energy absorbed per unit volume for the 3D assembly also cannot be achieved by summing that of its components. The energy absorption per unit volume is increased in the 3D core by more than the summed energy absorbing capacities for the 1D array and 2D cores (from  $2.79 \text{ MJm}^{-3}$  to  $10.4 \text{ MJm}^{-3}$ ), [Figure 14\(c\)](#). The energy absorbed per unit mass is also increased in the 3D core compared to the summed 1D array and 2D cores (from  $5.21 \text{ J/g}$  to  $19.2 \text{ J/g}$ ), [Figure 14\(c\)](#). [Table 4](#) summarizes the energy absorption values for the individual cores examined in this aspect of the study.

**4.5. Energy absorption comparisons.** The energy absorbed per unit mass for the 3D structures is plotted against the peak stress and compared to a selection of aluminum foams [[Chen 2001](#); [Miyoshi et al. 2000](#); [Hall et al. 2000](#)] and the upper bound limit for axially compressed square cross section tubes of various

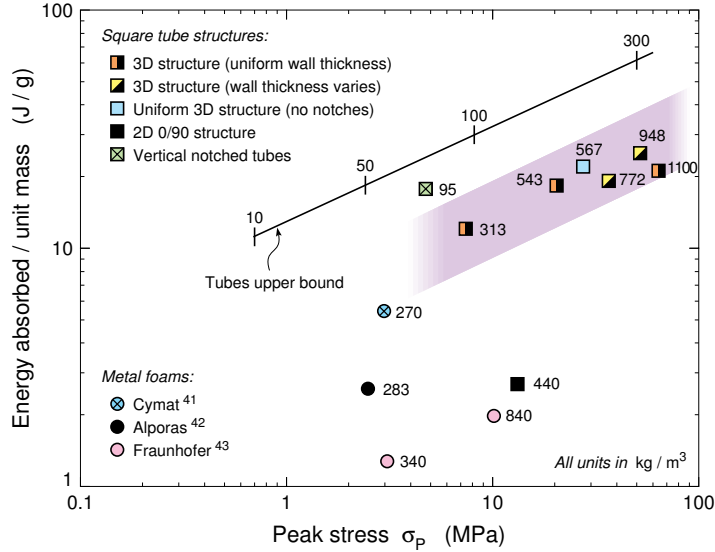


**Figure 15.** The energy absorbed per unit mass by the cellular structures investigated in this study compared to commercially available aluminum foams. Each cellular metal foam is labeled with its density in  $\text{kg/m}^3$ . The wall thickness to tube width ratio is shown for the tube upper bound relation.

wall thicknesses to tube width ratios; see Figure 15.<sup>1</sup> The line for the upper bound absorbed energy per unit mass,  $E_m$ , has been derived (see Appendix A) from the average crush force of tubular extrusions calculated in [Hanssen et al. 2001] as

$$E_m = \sigma_p \left[ \rho_s \frac{\sigma_p}{C_0 \sigma_0} \right]^{3/5} \quad (5)$$

where  $\sigma_0 = 0.5(\sigma_{02} + \sigma_u)$  is the extruded tube strength,  $\sigma_{02} = 278.2 \text{ MPa}$  is the nominal stress at 0.2% offset strain,  $\sigma_u = 310.5 \text{ MPa}$  is the ultimate tensile stress,  $\rho_s = 2700 \text{ kg}\cdot\text{m}^{-3}$  is the solid density of aluminum, and  $C_0 = 1.30$  is a coefficient for square tubes. Using the measured uniaxial tensile test results for the material studied here gives,  $\sigma_0 = 294.4 \text{ MPa}$ . Examination of Figure 15 shows that the 3D structures outperform all metal foams and falls just below the tube upper bound curve. It should be noted that the energy absorbed per unit mass for the unnotched vertical tubes fell just under the tube upper bound in Figure 15. We also note that unlike metal foams and arrays of axially compressed tubes which resist only crushing, the 3D structure has both excellent crush and stretch resistance.

## 5. Finite element investigation

Finite element techniques have been used to investigate the failure mechanisms responsible for the mechanical responses of the cellular structures.

<sup>1</sup>The energy absorption for the 3D structures and metal foams was always calculated by measuring the area under the stress-strain curve until the onset of densification (defined as the strain at which the stress reached that of the peak in crush strength).

**5.1. FE model.** All the finite element simulations were conducted using the explicit version of the commercial, nonlinear finite element package IMPETUS Afea Solver® [IMPETUS 2013]. The geometry and relative density of the modeled tube specimens was identical to those reported in Table 1. The initial models did not incorporate the defects in alignment and tube wall thickness seen in the experiments. The FE models were constructed using cubic hexahedral elements. A mesh sensitivity study indicated an in-plane nodal spacing approximately equal to the wall thickness ( $t$ ) was sufficient to provide converged solutions. One cubic hexahedral element was therefore used through the thickness of each tube wall. The nodes of the adjacent tubes were merged prior to the simulation, thus representing a perfect braze zone with no interface failure criterion. The contact formulation in the software is based on a penalty formulation. All the simulations used rigid front face sheets constrained by the general boundary condition option of IMPETUS Afea Solver to move only in the through thickness direction while the rigid back face sheet was clamped in all directions. The simulations were conducted by applying an out-of-plane velocity-time function,  $v(t)$ , to the front face sheet given by

$$v(t) = \frac{w}{t_{\text{end}}} \left( 1 - \cos \frac{360t}{t_{\text{end}}} \right) \quad (6)$$

where  $w$  is the crushing displacement of the sample (6 cm) and  $t_{\text{end}}$  is the end time for the loading (1 ms), which results in a maximum initial displacement rate of 6 m/s.

**5.2. Material properties.** The experimentally recovered Cauchy stress-true strain response of the 6061-T6 alloy undergoing uniaxial tensile testing was presented in Figure 7. The Cauchy stress,  $\sigma_c$ , versus true strain,  $\epsilon$ , relation for an elastic-plastic material under uniaxial straining can be written as

$$\epsilon = \epsilon_e + \epsilon_p = \frac{\sigma_c}{E} + \epsilon_p \quad (7)$$

where  $\epsilon_e$  and  $\epsilon_p$  are the elastic and plastic components of strain and  $E$  is Young's modulus. Having performed the uniaxial tensile test shown by Figure 7, the true stress vs. plastic strain curve was tabulated. From the true stress versus plastic strain curve, the hardening curve used for all FE simulations was extracted, and the true stress at 230.7 MPa was calibrated to zero plastic strain for the isotropic hardening assumption. This hardening tabulation was applied in IMPETUS Afea Solver using the general piecewise linear constitutive model prescription given by

$$\sigma_y = f(\epsilon_{\text{eff}}^P) \left( 1 - \left( \frac{T - T_0}{T_m - T_0} \right)^m \right) \left( 1 + \frac{\dot{\epsilon}_{\text{eff}}^P}{\epsilon_0} \right)^c \quad (8)$$

The piecewise linear hardening constitutive model option for IMPETUS-Afea Solver defined by Equation (8) includes thermal softening and strain rate hardening parts; however, these gave negligible contributions to the response and so for all tests, the yield stress was only defined by  $f(\epsilon_{\text{eff}}^P)$ , a piecewise linear function of the effective deviatoric strain, which was obtained from the hardening behavior. The 6061-T6 alloys constitutive response was modeled using a multiaxial von Mises yield criterion assuming isotropic hardening. The solid density  $\rho_s = 2700 \text{ kg}\cdot\text{m}^{-3}$ , Young's modulus  $E = 70.5 \text{ GPa}$ , and Poisson ratio  $\nu = 0.3$ . Using the material model described above, a uniaxial tensile test was simulated and compared to the measured Cauchy stress-logarithmic strain curve in Figure 7. The fit was good and these material properties were then used for all further simulations.

To account for softening created by tube wall fracture on the tensile side of severe buckles, the Cockcroft–Latham failure criterion [Cockcroft and Latham 1968] was implemented for all the compression simulations. This failure criterion is defined by a damage parameter,  $D = 1$ , calculated as

$$D = \frac{1}{W_c} \int_0^{\epsilon_{\text{eff}}^P} \max(0, \sigma_1) d\epsilon_{\text{eff}}^P \quad (9)$$

where  $\sigma_1$  is the first principle stress. The critical damage parameter,  $W_c = 85$  MPa was obtained by fitting the simulated measured stress-strain response of a single tube lateral compression test (Appendix B). The general node splitting feature in the IMPETUS code was turned on with the damage card and enabled failed nodes to split.

The 3D tube structure models were each built from 3,106 cubic hexahedra elements with 107,348 nodes. The wall thicknesses were homogenous throughout the meshed structures and their dimensions were set to match the 3D topologies in Table 1 with  $\bar{\rho} = 11.6\%$ ,  $\bar{\rho} = 20.1\%$ ,  $\bar{\rho} = 28.6\%$ ,  $\bar{\rho} = 35.1\%$ , and  $\bar{\rho} = 42.7\%$ . The perfectly aligned models gave much higher strengths than those seen in the experiments and so imperfections to the geometry of the FE models were introduced to trip buckling and provide a better fit to the measured stress-strain curves. The imperfections were modeled as a displacement of the lowest order measured eigenmode. The eigenmode amplitudes were altered by collecting all the internal tube wall faces with the general IMPETUS command used to define a surface from a seed node, and then pressurizing the 3D profiles from their inside walls using the general load pressure option of IMPETUS Afea Solver.

**5.3. Simulation results.** The simulated stress-strain curves are compared to the measured stress-strain compressive curves in Figures 12 and 13. First order eigenmode amplitudes of 2, 1.5, 2.6, 1.4 and 1.4 times the tube wall thickness were employed to trip buckling for the 11.6%, 20.1%, 28.6%, 35.1% and 42.7% relative density structures, respectively. These imperfection amplitudes are consistent with: (1) the significant misalignment of the 2D tubes at the boundary regions, (2) variations of tube wall thickness throughout the cellular structure, and (3) other random alignment errors as a result of tube slippage during dip brazing preparation. The laterally compressed tube simulations shown in Appendix B indicate that by alleviating these fabrication errors the need for large eigenmode amplitude imperfections can be avoided.

The collapse modes for each of the relative density samples are shown by Figure 16. The large initial eigenmode amplitudes are apparent in the early stages of strain, Figure 16(a)(i), (b)(i), and (c)(i). The strains in Figure 16 correspond to those shown in Figure 11, which also provide support for the large eigenmode imperfections introduced to the FE simulations. The buckling phenomenon observed during experiments (where the initial stress peak is controlled by through thickness tube buckling into a series of folds that initiate at the top of the tubes) is clearly observed in the simulations. Figure 17, for the 20.1% relative density structure, shows the buckling modes of the through thickness tubes in more detail by hiding two colinear tubes that block their view in Figure 16. In regions where the vertical tubes are not confined by the colinear tubes, the vertical tube walls buckle into the cavity spaces with a first order eigenmode in Figure 17(a). The notches at each through thickness layer nucleate the buckling of the through thickness tubes due to material failure (node splitting), shown in detail by Figure 18 (green tube at a strain of 3.7%). Figure 17(b) and (c) show that the vertical tubes buckle most intensely in the bottom

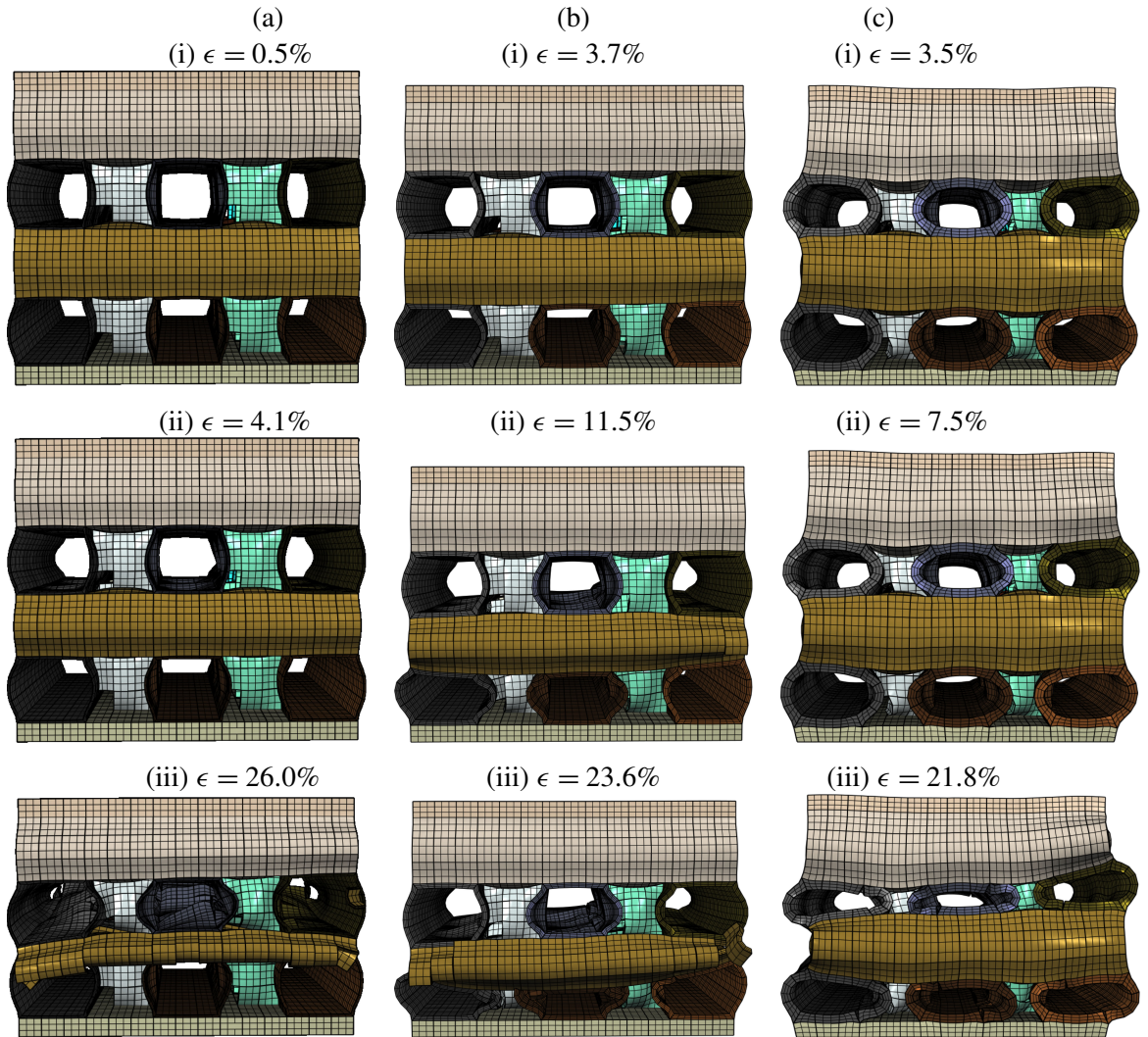


**Figure 16.** Images of the simulated collapse modes for 3D cellular structures with relative densities of (a) 11.6%, (b) 20.1%, and (c) 42.7%. The strain sequence corresponds to that of [Figure 11](#). The colors are used only to aid visualization of the deformations of each tube.

two layers of the structure, causing densification at this location first. As the vertical walls fold into the cavity spaces, the folds aid in crushing the colinear tubes below the folds.

The collapse modes in the void spaces (plane A in [Figure 18\(a\)](#)) can be seen in [Figure 18\(b\)](#), where all the walls buckle uniformly towards the void center as a result of reduced confinement. However, when all tube walls are brazed together at plane B ([Figure 18a](#)), nonuniform buckling of the colinear tubes side wall occurs on the side connected to the notch as a result of the notch collapse, [Figure 18\(c\)](#). The side of the colinear tube opposite the notch has a uniform collapse, but its first order eigenmode amplitude is less

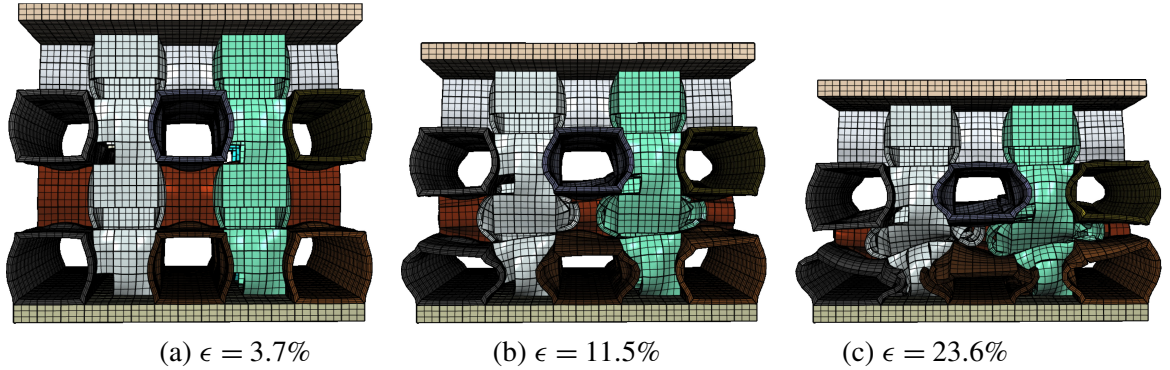


**Figure 17.** Images of the simulated collapse modes for 3D cellular structures with a relative density of 20.1%. Two colinear tubes have been hidden to show the collapse mode of the axial aligned tubes more clearly. The colors are used to improve visualization of the core deformations.

than the colinear tube that is not contained by the vertical tube, due to increased mass. In addition, the simulated densification strains exhibit a polynomial relationship upon relative density, by Equation (6).

The strength, modulus, and energy absorption of cellular foams was shown by Maiti et al. [1984], to be controlled by the relative density of the structure. This could be altered here by varying the tube wall thicknesses. Figure 19 shows that for relative densities between 11 and 42% the measured and predicted modulus of the 3D structures,  $E_{\text{cell}}$  scaled by that of the aluminum alloy,  $E_s$ , has a linear dependence upon relative density

$$E_{\text{cell}}/E_s = 3.6\bar{\rho}. \quad (10)$$

This is consistent with an initially stretch-dominated response [Hanssen et al. 1999]. The modulus of 3D orthogonal tube structures studied here is significantly higher than that of bending governed metal foams of similar relative density and material.

The peak strength of the 3D structure,  $\sigma_{\text{cell}}$ , scaled by the strength of the alloy from which it is made,  $\sigma_s$ , has a power dependence upon relative density

$$\sigma_{\text{cell}}/\sigma_s = 1.05(\bar{\rho})^{5/3}. \quad (11)$$

Using an energy balance argument, Wierzbicki and Abramowicz [1983] showed that the average axial crushing stress for an array of vertical tubes scaled with relative density to the power 5/3. This seems to agree well with both the experimental data and FE predictions presented here for the 3D structures whose response is dominated by the vertical tubes. We note that the 2D structure (which contains no vertical tubes aligned with the loading direction) deforms by transverse tube crushing and is expected to be a bending dominated system whose strength will scale with relative density to the power 3/2 like open cell foams, which are also bending dominated structures [Maiti et al. 1984].

Table 5 summarizes the energy absorption for the simulated 3D structures. A comparison of Tables 4 and 5 shows only small differences between the measured and simulated energy absorptions. The insignificant deviations demonstrate the good predictive accuracy of the simulations. However, the energy absorption efficiency showed more significant variability between measurements and simulations. This

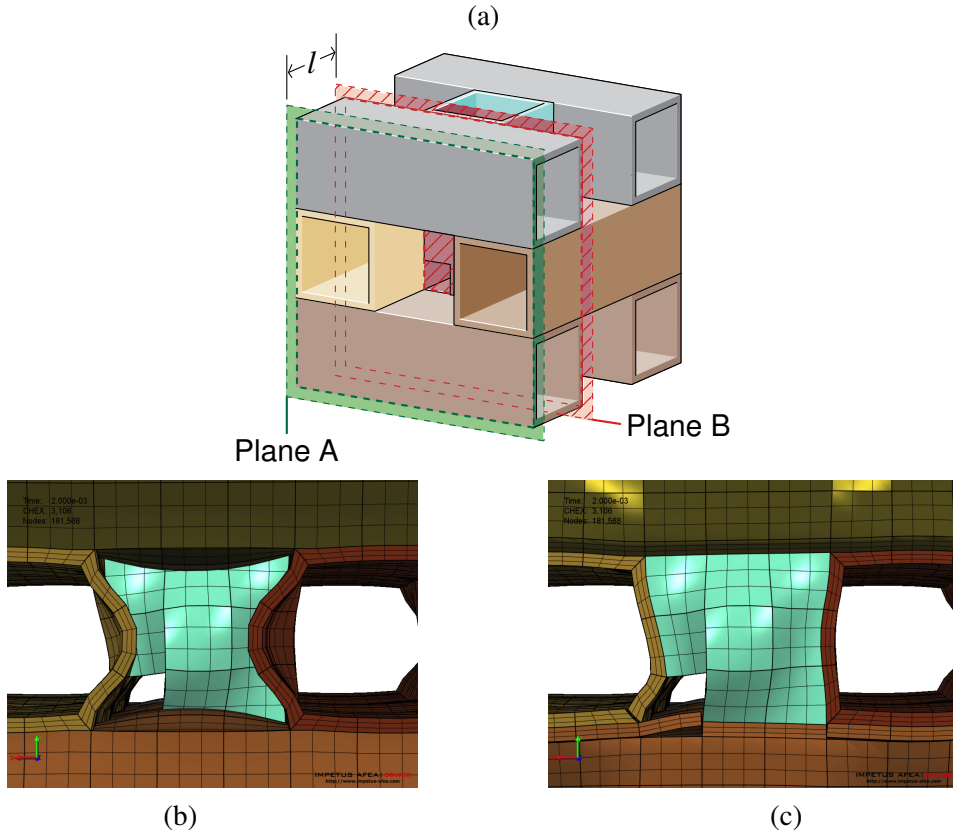


**Figure 18.** Simulated images of the collapse mode of a notched 3D cellular structure with a relative density of 20.1%. (a) Location of image planes. (b) In-plane tube wall buckling at Plane A. (c) Buckling on Plane B located deeper within the sample. Note the constraint imposed by the vertical tube upon the amplitude of the in-plane tube buckling mode.

Topology	Relative density, $\bar{\rho}$	Peak stress, $\sigma_p$ (MPa)	$\epsilon_D$	$E_v$ (MJ/m <sup>3</sup> )	$E_m$ (J/g)	Theoretical $E_m$ (J/g)	Energy absorbing efficiency
3D	42.7	62.0	0.49	25.7	22.3	22.7	0.97
3D	35.1	53.8	0.45	21.0	22.1	23.1	0.95
3D	28.6	36.0	0.47	15.7	20.3	20.6	0.98
3D	20.1	20.7	0.64	10.9	20.3	23.6	0.85
3D	11.6	7.3	0.70	3.5	11.2	16.4	0.68

**Table 5.** Energy absorption values for simulated 3D structures.

arose because of the *product* of the simulated densification strain and peak strength was less accurately estimated.

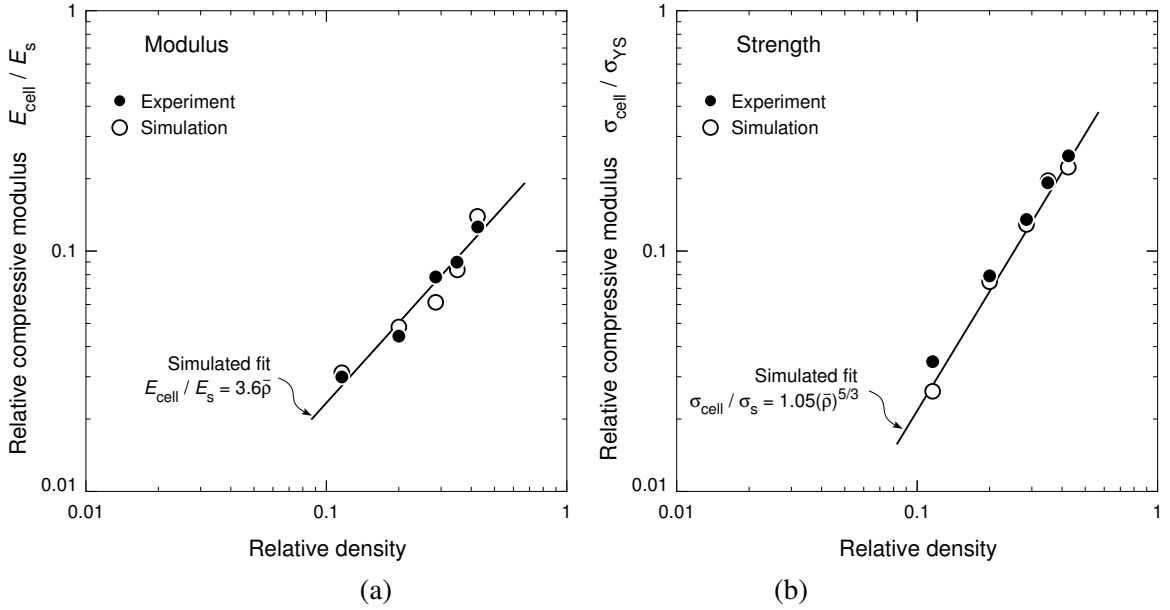


**Figure 19.** Dependence of (a) compressive modulus and (b) compressive strength upon relative density. Empirical fits to the data are also shown.

## 6. Summary

Three-dimensional orthogonal tube cellular structures for impact mitigation applications have been manufactured by dip brazing square extruded tubes made of aluminum alloy 6061 and heat treating the structure to the peak aged condition. The 3D structures material is orthotropic and the out-of-plane compressive response of structures with relative densities between 10 and 40% was measured and numerically simulated to investigate the mechanisms of plastic collapse and mechanical energy storage. We find that:

- (1) The elastic modulus has an approximately linear dependence on relative density, given by  $E_{\text{cell}}/E_s = 3.6\bar{\rho}$ , consistent with an initially stretch dominated response. The modulus of 3D orthogonal tube structures is significantly higher than metal foams of similar relative density and material.
- (2) The peak strength exhibits a power law dependence upon relative density, given by  $\sigma_{\text{cell}}/\sigma_s = 1.05(\bar{\rho})^{5/3}$ . In-situ experimental observations and finite element simulations reveal the crush strength to be controlled by buckling of tubes oriented in the applied load direction.
- (3) The specific energy absorption increased with compressive strength from about 10 kJ/kg at a compressive strength of about 10 MPa to 30 kJ/kg at strengths of about 60 MPa. This was slightly less than the specific strength of arrays of vertical tubes, but this was off-set by the existence of a nonzero in-plane compressive strength. In addition, the colinear aligned tubes should provide the structure with good stretch resistance, which is equally important for impact applications.

### Appendix A. Tube upper bound derivation

The axial crushing of both square [Hanssen et al. 1999] and circular [Hanssen et al. 2000b] tubes has been widely studied. The expression for the average crush force for a hollow extrusion is given by the design formula [Jones 1989]

$$F_{\text{avg}}^0 = C_0 \phi^{2/3} \sigma_0 A_s. \quad (12)$$

The parameters involved are:

$C_0$ : cross section dependent dimensionless constant.

$\phi = A_s/A_f$ : solidity ratio, where  $A_s$  is the solid (net) extrusion cross section and  $A_f$  the gross cross section area.

$\sigma_0 = 0.5(\sigma_{02} + \sigma_u)$ : characteristic stress of extrusion material, where  $\sigma_{02}$  is the nominal stress at 0.2% plastic strain, and  $\sigma_u$  is the ultimate nominal stress.

The compressive peak stress for a crushed extruded tube is described as the average crush force over the tubes gross cross sectional area. Starting from Equation (12), the compressive peak stress is defined by

$$\sigma_p = \frac{F_{\text{avg}}^0}{A_f} = C_0 \phi^{5/3} \sigma_0. \quad (13)$$

Parameters in Equation (13) can be organized to redefine  $\phi$ , with measurable values, as

$$\phi = \left( \frac{\sigma_p}{C_0 \sigma_0} \right)^{3/5}. \quad (14)$$

The energy absorbed ( $E$ ) by the crushed extruded tube is dependent on the average crush force and the tubes axial displacement ( $w$ ), and is written as

$$E = F_{\text{avg}}^0 w. \quad (15)$$

This energy absorbed per unit crush mass ( $E_m$ ) is described by

$$E_m = \frac{F_{\text{avg}}^0 w}{\rho_s A_s w} = \frac{F_{\text{avg}}^0}{\rho_s A_s} \quad (16)$$

where  $\rho_s$  is the density of the tube material. The ratio for the tube energy absorbed per unit mass, Equation (16), over the tube peak stress, Equation (13), is expressed by

$$\frac{E_m}{\sigma_p} = \frac{F_{\text{avg}}^0 / (\rho_s A_s)}{F_{\text{avg}}^0 / A_f} = \frac{A_f}{\rho_s A_s} = \frac{1}{\rho_s \phi}. \quad (17)$$

Rearranging (17) to define the tube energy absorbed per unit mass ( $E_m$ ) with respect to the tube peak stress ( $\sigma_p$ ) and substituting  $\phi$  with (14) results in the expression used to graphically obtain the tube upper limit shown in Figure 15 as

$$E_m = \frac{\sigma_p}{\rho_s \phi} = \sigma_p \left( \rho_s \frac{\sigma_p}{C_0 \sigma_0} \right)^{3/5}. \quad (18)$$

	Measured	Numerical model
Top wall thickness (mm)	1.59	1.575
Right wall thickness (mm)	1.57	1.575
Left wall thickness (mm)	1.58	1.575
Bottom wall thickness (mm)	1.58	1.575
Right to left wall outer width (mm)	18.99	19.05
Top to bottom wall outer width (mm)	18.95	19.05
Relative density, $\bar{\rho}$	28.74	30.34
Peak stress, $\sigma_p$ (MPa)	48.83	49.15

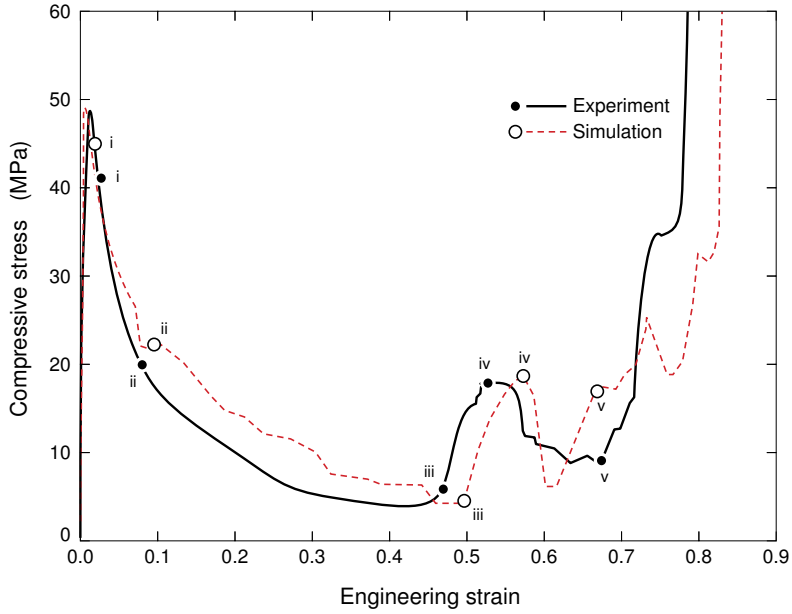
**Table 6.** Measured dimensions of single tube profile sample studied under quasistatic compressive lateral loading.

### Appendix B. Lateral compression of a single tube

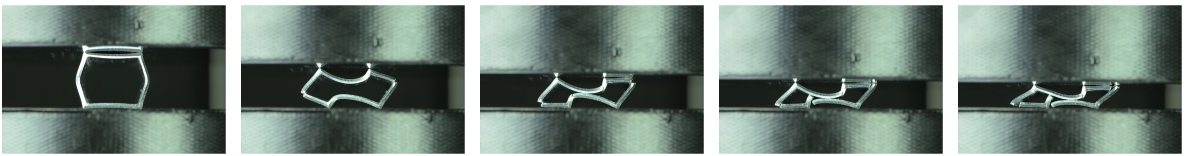
To test the validity of the modeling approach prior to simulating quasistatic compression of the 3D topologies we set up a simple single square tube compression experiment and compared the measured and simulated response using the material model described above. We also tuned the critical damage parameter ( $W_c$ ) with this simulation to 85 MPa, which was applied to all 3D simulations to initiate node splitting.

The dimensions of the measured and modeled tube are outlined in [Table 6](#). The tested tube underwent the same thermal processes as outlined in [Section 2.2](#), rendering an age-hardened AA 6061-T6 tube. The Specimen was compressed in a 50 kN Instron universal testing machine (Instron Corporation, Model 4208, Canton, MA, USA) at a strain rate of  $\dot{\epsilon} = 4 \times 10^{-3} \text{ s}^{-1}$  and temperature of 25°C. A laser extensometer (Electronic Instrument Research, Model LE-01, Irwin, PA, USA) was used to measure the displacement of the tube walls. It should be noted that the tube was not brazed to a face sheet material like the 3D orthogonal tube samples in the study. Instead, the tube walls directly contacted the load platens, which resulted in a different collapse mode to that of tubes that were brazed to face sheets.

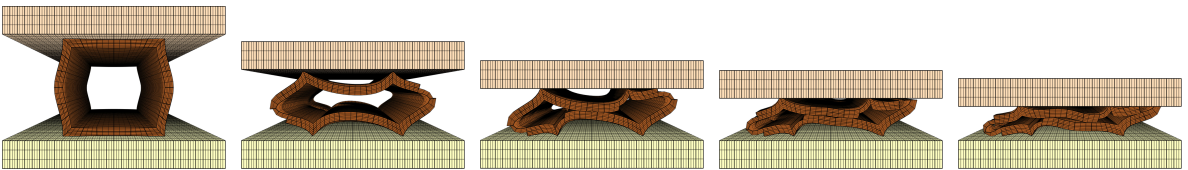
The meshed tube structure was built from 3,240 cubic hexahedra elements with 112,112 nodes. The simulated stress-strain curve in [Figure 19](#) demonstrates a good fit to the measured sample. A comparison of [Figure 20\(b\)](#) and (c) shows near identical collapse mode predictions for the experimental and simulated single tube profiles. Thus, the material properties were deemed satisfactory for the 3D orthogonal tube assemblies. Besides providing verification of the material approach, this model also provided evidence of the sensitivity between tube wall thickness and predicting the force curves. No imperfections were necessary with a single tube since the wall thickness of the numerical models fell within 1% or less of each other. This observation suggests that there was a combination of 1) variability in the thickness of each tube that formed the 3D structure and 2) the misalignment caused by fabrication resulted in the large imperfections that were required to trip the simulated 3D structures buckling.



(a)



(i) (ii) (iii) (iv) (v)  
(b)



(i) (ii) (iii) (iv) (v)  
(c)

**Figure 20.** (a) A stress-strain curve for a single tube under lateral compression. (b) The experimentally observed sequence of the tested collapse modes. (c) The sequence of simulated collapse modes.

### Acknowledgements

The authors are grateful to the U.S. Office of Naval Research (ONR grant number N00014-07-1-0764) for financial support of this research.

## References

- [Allen 1969] H. G. Allen, *Analysis and design of structural sandwich panels*, Pergamon, Oxford, 1969.
- [ASM 2003] *Brazing of aluminum alloys*, pp. 627–1067, ASM International, Materials Park, OH, 2003.
- [Baumeister et al. 1997] J. Baumeister, J. Banhart, and M. Weber, “Aluminium foams for transport industry”, *Mater. Des.* **18**:4-6 (1997), 217–220.
- [Bitzer 1997] T. Bitzer, *Honeycomb technology*, Chapman and Hall, London, 1997.
- [Braithwaite 2008] D. Braithwaite, 2008, <http://www.colemanmw.com>. Personal communication.
- [Chakrabarti and Laughlin 2004] D. J. Chakrabarti and D. E. Laughlin, “Phase relations and precipitation in Al-Mg-Si alloys with Cu additions”, *Prog. Mater. Sci.* **49**:3-4 (2004), 389–410.
- [Chen 2001] W. Chen, “Experimental and numerical study on bending collapse of aluminum foam-filled hat profiles”, *Int. J. Solids Struct.* **38**:44-45 (2001), 7919–7944.
- [Cockcroft and Latham 1968] M. G. Cockcroft and D. J. Latham, “Ductility and workability of metals”, *J. Inst. Met.* **96** (1968), 33–39.
- [Dharmasena et al. 2008] K. P. Dharmasena, H. N. G. Wadley, Z. Xue, and J. W. Hutchinson, “Mechanical response of metallic honeycomb sandwich panel structures to high intensity dynamic loading”, *Int. J. Impact Eng.* **35** (2008), 1063–1074.
- [Elzey and Wadley 2001] D. M. Elzey and H. N. G. Wadley, “The limits of solid state foaming”, *Acta Mater.* **49** (2001), 849–859.
- [Evans et al. 2001] A. G. Evans, J. W. Hutchinson, N. A. Fleck, M. F. Ashby, and H. N. G. Wadley, “The topological design of multifunctional cellular metals”, *Prog. Mater. Sci.* **46** (2001), 309–327.
- [Finnegan et al. 2007] K. Finnegan, G. Kooistra, H. N. G. Wadley, and V. S. Deshpande, “The compressive response of carbon fiber composite pyramidal truss sandwich cores”, *Int. J. Mater. Res.* **12** (2007), 1264–1272.
- [Fleming et al. 2012] K. Fleming, A. Zhu, and J. Scully, “Corrosion of AA6061 brazed with an Al-Si alloy: effects of Si on metallurgical and corrosion behavior”, *Corros. J. Sci. Eng.* **68**:12 (2012), 1126–1145.
- [Gibson and Ashby 1988] L. J. Gibson and M. F. Ashby, *Cellular solids: structure and properties*, Pergamon, Oxford, 1988.
- [Gibson and Ashby 1997] L. J. Gibson and M. F. Ashby, *Cellular solids: structure and properties*, 2nd ed., Cambridge University Press, Cambridge, 1997.
- [Hall et al. 2000] I. W. Hall, M. Guden, and C.-J. Yu, “Crushing of aluminum closed cell foams: density and strain rate effects”, *Scr. Mater.* **43** (2000), 515–521.
- [Hanssen et al. 1999] A. G. Hanssen, M. Langseth, and O. S. Hopperstad, “Static crushing of square aluminium extrusions with aluminium foam filler”, *Int. J. Mech. Sci.* **41** (1999), 967–993.
- [Hanssen et al. 2000a] A. G. Hanssen, M. Langseth, and O. S. Hopperstad, “Static and dynamic crushing of square aluminium extrusions with aluminium foam filler”, *Int. J. Impact Eng.* **24**:4 (2000), 347–383.
- [Hanssen et al. 2000b] A. G. Hanssen, M. Langseth, and O. S. Hopperstad, “Static and dynamic crushing of circular aluminium extrusions with aluminium foam filler”, *Int. J. Impact Eng.* **24**:5 (2000), 475–507.
- [Hanssen et al. 2001] A. G. Hanssen, O. S. Hopperstad, and M. Langseth, “Design of aluminium foam-filled crash boxes with square and circular cross sections”, *Int. J. Crashworthiness* **6**:2 (2001), 177–188.
- [Hatch 1984] J. E. Hatch (editor), *Aluminum: properties and physical metallurgy*, pp. 226–293, American Society for Metals, Metals Park, OH, 1984.
- [Hutchinson and Xue 2005] J. W. Hutchinson and Z. Y. Xue, “Metal sandwich plates optimized for pressure impulses”, *Int. J. Mech. Sci.* **47**:4-5 (2005), 545–556.
- [IMPETUS 2013] IMPETUS, “IMPETUS Afea Solver®”, 2013, <http://www.impetus-afea.com>.
- [Jones 1989] N. Jones, *Structural impact*, Cambridge University Press, Cambridge, 1989. 2nd ed. in 2012.
- [Kooistra et al. 2004] G. W. Kooistra, V. S. Deshpande, and H. N. G. Wadley, “Compressive behavior of age hardenable tetrahedral lattice truss structures made from aluminium”, *Acta Mater.* **52**:14 (2004), 4299–4237.

- [Kooistra et al. 2008] G. W. Kooistra, D. T. Queheillalt, and H. N. G. Wadley, “Shear behavior of aluminum lattice truss sandwich panel structures”, *Mater. Sci. Eng. A* **472** (2008), 242–250.
- [Laurin and Vizzini 2005] F. Laurin and A. J. Vizzini, “Energy absorption of sandwich panels with composite-reinforced foam core”, *J. Sandw. Struct. Mater.* **7** (2005), 113–132.
- [Liang et al. 2007] Y. Liang, A. V. Spuskanyuk, S. E. Flores, D. R. Hayhurst, J. W. Hutchinson, R. M. McMeeking, and A. G. Evans, “The response of metallic sandwich panels to water blast”, *J. Appl. Mech. (ASME)* **74** (2007), 81–99.
- [Maiti et al. 1984] S. K. Maiti, L. J. Gibson, and M. F. Ashby, “Deformation and energy absorption diagrams for cellular solids”, *Acta Metall.* **32**:11 (1984), 1963–1975.
- [McShane et al. 2007] G. J. McShane, D. D. Radford, V. S. Deshpande, and N. A. Fleck, “The dynamic compressive response of square-honeycombs”, *J. Appl. Mech. (ASME)* **74** (2007), 658–667.
- [Mills 2007] N. J. Mills, “Polyurethane foams: processing and microstructure”, Chapter 2, pp. 19–37 in *Polymer foams handbook: engineering and biomechanics applications and design guide*, Butterworth-Heinemann, Amsterdam, 2007.
- [Miyoshi et al. 2000] T. Miyoshi, M. Itah, S. Akiyama, and A. Kitahara, “ALPORAS aluminum foam: production process, properties, and applications”, *Adv. Eng. Mater.* **2**:4 (2000), 179–183.
- [Moongkhamklang and Wadley 2010] P. Moongkhamklang and H. N. G. Wadley, “Titanium alloy lattice structures with millimeter scale cell sizes”, *Adv. Eng. Mater.* **12**:11 (2010), 1111–1116.
- [Queheillalt et al. 2000] D. T. Queheillalt, B. W. Choi, H. N. G. Wadley, and D. S. Schwartz, “Creep expansion of porous Ti-6Al-4V sandwich structures”, *Metall. Trans. A* **31** (2000), 261–273.
- [Queheillalt et al. 2008] D. T. Queheillalt, Y. Murty, and H. N. G. Wadley, “Mechanical properties of an extruded pyramidal lattice truss sandwich structure”, *Scr. Mater.* **58**:1 (2008), 76–79.
- [Reid 1993] S. R. Reid, “Plastic deformation mechanisms in axially compressed metal tubes used as impact energy absorbers”, *Int. J. Mech. Sci.* **35**:12 (1993), 1035–1052.
- [Reyes 2008] G. Reyes, “Static and low velocity impact behavior of composite sandwich panels with an aluminum foam core”, *J. Compos. Mater.* **42**:16 (2008), 1659–1670.
- [Rimoli et al. 2011] J. J. Rimoli, B. Talamini, J. J. Wetzel, K. P. Dharmasena, R. Radovitzky, and H. N. G. Wadley, “Wet-sand impulse loading of metallic plates and corrugated core sandwich panels”, *Int. J. Impact Eng.* **38** (2011), 837–848.
- [Russell et al. 2008] B. Russell, V. S. Deshpande, and H. N. G. Wadley, “Quasistatic deformation and failure modes of composite square honeycombs”, *J. Mech. Mater. Struct.* **3**:7 (2008), 1315–1340.
- [Tian et al. 2007] J. Tian, T. J. Lu, H. P. Hodson, D. T. Queheillalt, and H. N. G. Wadley, “Cross flow heat exchange of textile cellular metal core sandwich panels”, *Int. J. Heat Mass Transf.* **50** (2007), 2521–2536.
- [Tilbrook et al. 2006] M. T. Tilbrook, V. S. Deshpande, and N. A. Fleck, “The impulsive response of sandwich beams: analytical and numerical investigation of regimes of behavior”, *J. Mech. Phys. Solids* **54** (2006), 2242–2280.
- [Vaziri et al. 2007] A. Vaziri, Z. Xue, and J. W. Hutchinson, “Performance and failure of metal sandwich plates subjected to shock loading”, *J. Mech. Mater. Struct.* **2**:10 (2007), 1947–1963.
- [Vinson 2001] J. R. Vinson, “Sandwich structures”, *Appl. Mech. Rev. (ASME)* **54**:3 (2001), 201–214.
- [Wadley 2006] H. N. G. Wadley, “Multifunctional periodic cellular metals”, *Phil. Trans. R. Soc. A* **364**:1838 (2006), 31–68.
- [Wadley et al. 2007] H. N. G. Wadley, K. P. Dharmasena, D. T. Queheillalt, Y. Chen, P. Dudt, D. Knight, K. Kiddy, Z. Xue, and A. Vaziri, “Dynamic compression of square honeycomb structures during underwater impulsive loading”, *J. Mech. Mater. Struct.* **2**:10 (2007), 2025–2048.
- [Wei et al. 2007] Z. Wei, K. P. Dharmasena, H. N. G. Wadley, and A. G. Evans, “Analysis and interpretation of a test for characterizing the response of sandwich panels to water blast”, *Int. J. Impact Eng.* **34** (2007), 1602–1618.
- [Wei et al. 2008] Z. Wei, V. S. Deshpande, A. G. Evans, K. P. Dharmasena, D. T. Queheillalt, H. N. G. Wadley, Y. Murty, R. K. Elzey, P. Dudt, Y. Chen, D. Knight, and K. Kiddy, “The resistance of metallic plates to localized impulse”, *J. Mech. Phys. Solids* **56** (2008), 2074–2091.
- [Wicks and Hutchinson 2001] N. Wicks and J. W. Hutchinson, “Optimal truss plates”, *Int. J. Solids Struct.* **38** (2001), 5165–5183.

[Wierzbicki and Abramowicz 1983] T. Wierzbicki and W. Abramowicz, “On the crushing mechanics of thin-walled structures”, *J. Appl. Mech. (ASME)* **50** (1983), 727–739.

[Xue and Hutchinson 2006] Z. Xue and J. W. Hutchinson, “Crush dynamics of square honeycomb sandwich cores”, *Int. J. Numer. Methods Eng.* **65** (2006), 2221–2245.

[Zenkert 1995] D. Zenkert, *An introduction to sandwich construction*, Chameleon, London, 1995.

Received 4 Sep 2012. Revised 19 Oct 2012. Accepted 30 Oct 2012.

RYAN L. HOLLOMAN: [rlh5v@virginia.edu](mailto:rlh5v@virginia.edu)

*Department of Materials Science and Engineering, University of Virginia, Charlottesville, VA 22903, United States*

VIKRAM DESHPANDE: [vsd20@cam.ac.uk](mailto:vsd20@cam.ac.uk)

*Engineering Department, University of Cambridge, Trumpington Street, Cambridge, CB2 1PZ, United Kingdom*

ARVE G. HANSEN: [arve@impetus.no](mailto:arve@impetus.no)

*IMPETUS Afea AS, Strandgaten 32, N-4400 Flekkefjord, Norway*

KATHERINE M. FLEMING: [kmf2m@virginia.edu](mailto:kmf2m@virginia.edu)

*Department of Materials Science and Engineering, University of Virginia, Charlottesville, VA 22903, United States*

JOHN R. SCULLY: [jrs8d@virginia.edu](mailto:jrs8d@virginia.edu)

*Department of Materials Science and Engineering, University of Virginia, Charlottesville, VA 22903, United States*  
<http://www.virginia.edu/cese/>

HAYDN N. G. WADLEY: [haydn@virginia.edu](mailto:haydn@virginia.edu)

*Department of Materials Science and Engineering, University of Virginia, Charlottesville, VA 22903, United States*  
<http://www.ipm.virginia.edu/>

# JOURNAL OF MECHANICS OF MATERIALS AND STRUCTURES

[msp.org/jomms](http://msp.org/jomms)

Founded by Charles R. Steele and Marie-Louise Steele

## EDITORS

CHARLES R. STEELE Stanford University, USA  
DAVIDE BIGONI University of Trento, Italy  
IWONA JASIUK University of Illinois at Urbana-Champaign, USA  
YASUHIRO SHINDO Tohoku University, Japan

## EDITORIAL BOARD

H. D. BUI École Polytechnique, France  
J. P. CARTER University of Sydney, Australia  
R. M. CHRISTENSEN Stanford University, USA  
G. M. L. GLADWELL University of Waterloo, Canada  
D. H. HODGES Georgia Institute of Technology, USA  
J. HUTCHINSON Harvard University, USA  
C. HWU National Cheng Kung University, Taiwan  
B. L. KARIHALOO University of Wales, UK  
Y. Y. KIM Seoul National University, Republic of Korea  
Z. MROZ Academy of Science, Poland  
D. PAMPLONA Universidade Católica do Rio de Janeiro, Brazil  
M. B. RUBIN Technion, Haifa, Israel  
A. N. SHUPIKOV Ukrainian Academy of Sciences, Ukraine  
T. TARNAI University Budapest, Hungary  
F. Y. M. WAN University of California, Irvine, USA  
P. WRIGGERS Universität Hannover, Germany  
W. YANG Tsinghua University, China  
F. ZIEGLER Technische Universität Wien, Austria

**PRODUCTION** [production@msp.org](mailto:production@msp.org)

SILVIO LEVY Scientific Editor

Cover photo: Ev Shafir

---

See [msp.org/jomms](http://msp.org/jomms) for submission guidelines.

JoMMS (ISSN 1559-3959) at Mathematical Sciences Publishers, 798 Evans Hall #6840, c/o University of California, Berkeley, CA 94720-3840, is published in 10 issues a year. The subscription price for 2013 is US\$555/year for the electronic version, and \$705/year (+\$60, if shipping outside the US) for print and electronic. Subscriptions, requests for back issues, and changes of address should be sent to MSP.

---

JoMMS peer-review and production is managed by EditFLOW® from Mathematical Sciences Publishers.

PUBLISHED BY

 **mathematical sciences publishers**

**nonprofit scientific publishing**

<http://msp.org/>

© 2013 Mathematical Sciences Publishers

<b>Numerical and experimental investigation of the dynamic characteristics of cable-supported barrel vault structures</b>	<b>SUN GUO-JUN, CHEN ZHI-HUA and RICHARD W. LONGMAN</b>	<b>1</b>
<b>When beam theories fail</b>	<b>PAUL R. HEYLIGER</b>	<b>15</b>
<b>Transient 3D singular solutions for use in problems of prestressed highly elastic solids</b>	<b>LOUIS MILTON BROCK</b>	<b>37</b>
<b>Wave velocity formulas to evaluate elastic constants of soft biological tissues</b>	<b>PHAM CHI VINH and JOSE MERODIO</b>	<b>51</b>
<b>Tubular aluminum cellular structures: fabrication and mechanical response</b>	<b>RYAN L. HOLLOMAN, VIKRAM DESHPANDE, ARVE G. HANSEN, KATHERINE M. FLEMING, JOHN R. SCULLY and HAYDN N. G. WADLEY</b>	<b>65</b>
<b>Reflection of plane longitudinal waves from the stress-free boundary of a nonlocal, micropolar solid half-space</b>	<b>AARTI KHURANA and SUSHIL K. TOMAR</b>	<b>95</b>